HHS Public Access

Author manuscript

Angew Chem Int Ed Engl. Author manuscript; available in PMC 2021 May 11.

Published in final edited form as:

Angew Chem Int Ed Engl. 2020 May 11; 59(20): 7678–7699. doi:10.1002/anie.201907502.

Catalysis and Electron Transfer in *De Novo* Designed Helical Scaffolds

Tyler B. J. Pinter[†], **Karl J. Koebke**[†], **Vincent L. Pecoraro**[†,*]

[†]Department of Chemistry, University of Michigan, Ann Arbor, Michigan, United States, 48109-1055

Abstract

The relationship between protein structure and function is one of the greatest puzzles within biochemistry. *De novo* metalloprotein design is a way to wipe the board clean and determine what is required to build in function from the ground up in an unrelated structure. This review focuses on protein design efforts to create *de novo* metalloproteins within alpha helical scaffolds. Examples of successful designs from our lab include those with carbonic anhydrase or nitrite reductase activity by incorporating a $ZnHis_3$ or $CuHis_3$ site, or that recapitulate the spectroscopy of unique electron transfer sites from cupredoxins ($CuHis_2Cys$) to rubredoxin ($FeCys_4$). This work showcases the versatility of alpha helices as scaffolds for metalloprotein design and the progress that is possible through careful rational design as we show the invariance of carbonic anhydrase activity to site position and scaffold, refine our cupredoxin models, and enhance nitrite reductase activity up to 1000-fold.

Graphical Abstract

[*]Corresponding Author: vlpec@umich.edu.

The authors declare no competing interests.

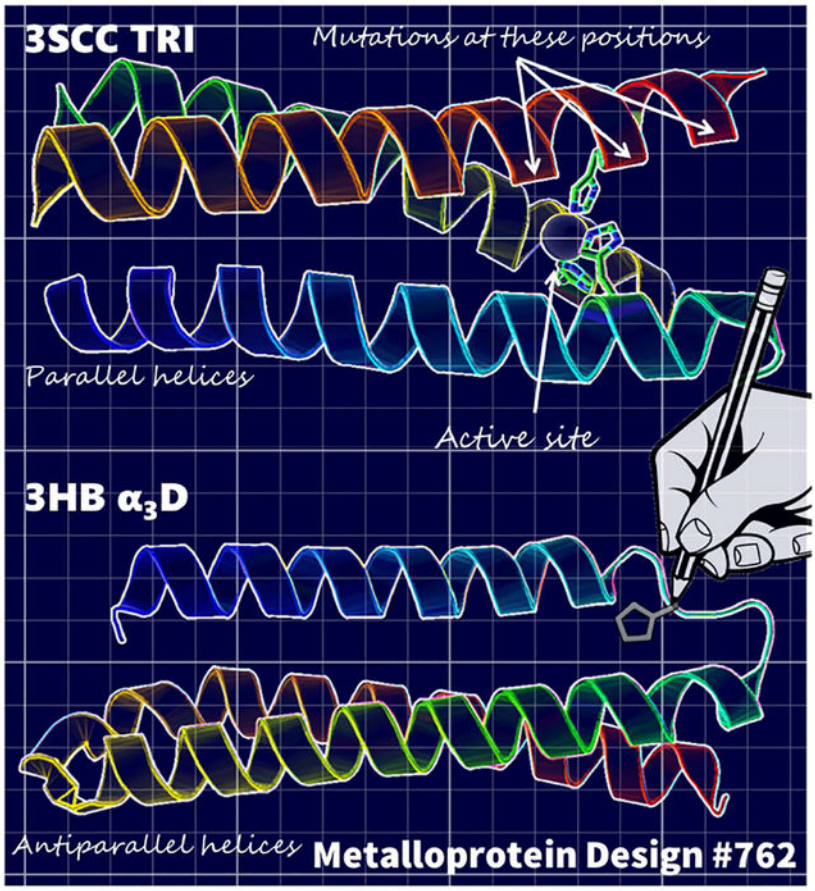

Keywords

Bioinorganic chemistry; Protein design; Transition metals; Enzymes; Helical Structures; Metalloproteins

1. Introduction

Metalloproteins and peptides perform an immense number of the most critically important biochemical reactions required for all life.[1] Some of the most significant of these are the transfer of electrons within biological systems using redox active metal centers and protein-supported metal-facilitated catalysis.[1c, 2] Such significance highlights the extensive and wide field of metals in biology research that can be tapped to aid in the development of *de novo* designed systems.

De novo protein design uses a bottom-up approach to the development of a functional protein in folds completely different from the native systems.[3] Such a strategy has two equally important and parallel goals. The first goal is that, through recapitulation of native metal binding sites in *de novo* scaffolds which generally possess a significantly different secondary structure than the native system, we are challenging the accuracy and completeness of our understanding of chemical principles and properties that govern

metalloprotein function. This approach allows one to examine the base requirements of the desired function being studied, without the additional potentially convoluting 'evolutionary baggage' that accompanies the study of native proteins.[4] The second goal is to generate novel catalysts that have improved properties for catalytic applications.[5] There are numerous approaches to *de novo* designing a metalloprotein and an even larger number of designed scaffolds to work with.[6] There have been many reviews on the subject of metalloprotein design for catalysis[3e] including an entire issue of *Accounts of Chemical Research*. Therefore, this review highlights recent developments using purely alpha-helical structure, specifically using three-stranded coiled coils (3SCCs) peptides and three helix bundle (3HB) proteins, emphasizing research from our group.

There are several advantages to 3SCCs and 3HB systems.[7] The TRI family of 3SCCs is designed from CoilSer[8] which itself originated from the polyheptapeptide designed by Hodges et. Al. to mimic coiled-coil tropomycin.[9] TRI consists of repeating heptads (*abcdefg*) with leucine residues in the first (*a*-site) and fourth (*d*-site) positions.[10] The other positions are helix inducing (Ala, *c*-sites), charged and/or salt bridging residues (Lys *b,g* and Glu *e,f,*-sites). The geometry of a super-coiled alpha helix, with 3.5 residues per turn aligns the leucine residues on one face of the alpha-helix, creating an amphiphilic structure. The crystallographic analogue or TRI, CoilSer (CS) is shown in Figure 1A. In TRI, three alpha-helixes associate in a parallel manner and the leucine residues pack together to form a hydrophobic core of *a* and *d* residues. Salt bridges between *e* and *f* residues on neighboring strands stabilize the structure. To enhance coiled-coil stability, the N-terminus and C-terminus are amidated and acylated, respectively. This arrangement creates layers of leucine residues in the core that can be substituted for metal binding residues to generate metal binding sites within the TRI scaffold. Table 1 lists the sequences of CS and TRI peptides that will be discussed in this review.

Three parallel and independent strands must associate in the TRI/CS system to form a metal binding site. This differs significantly from most native metal binding sites where the metal chelating residues are all from the same strand. Therefore, a second scaffold was created that links the three alpha-helixes together using flexible loops to create α_3D, an antiparallel 3HB protein, Figure 1B. However, the *de novo* design strategy remains the same as for TRI, substitution of hydrophobic core residues or residues near or on the flexible loops for metal-binding residues generates metal binding sites. An additional distinction between TRI and α_3D is that since TRI is formed by the association of three identical strands, only symmetric metal binding sites can be generated. In α_3D, however, each amino acid can independently be mutated, allowing complete control of the residues around and within the metal coordination sphere. Finally, in order to increase stability of the 3HB scaffold with increasing number of destabilizing mutations to the parent scaffold (*vida infra*), we designed a lengthened version called Grand α_3D (GRα_3D, Figure 1C).[11] In this review, we will describe advances that we have made towards the rational design of both catalytic and electron transfer metal binding sites within our TRI (including TRI, GRAND and CoilSer peptides) and α_3D scaffolds (including α_3D and Grand α_3D).

2. De novo designed metallopeptides for catalysis

Metals in biology catalyze an extremely diverse set of reactions.[14] The same metal in different peptidic environments can possess wildly varying activities and display disparate chemistries. Iron, for example, plays critical roles in oxygen storage and transport, electron transfer, and numerous hydroxylation, dioxygenation, oxidation and hydrolysis reactions; each chemistry being modulated only by the specific environment in which the metal is located.[15] Thus, by approximate recreation of the position of specific conserved residues that surround native metal binding sites, we are able to generate desired catalytic activities in our *de novo* scaffolds. There are three functions that we have had the most success with to date, zinc catalyzed hydrolytic, nitrite reductase activities, and electron transfer sites.

2.1 Development of zinc sites as models of carbonic anhydrase hydrolytic activity

Building upon our wealth of knowledge of heavy metal binding to tris(cysteine) layers in our *de novo* designed scaffolds,[16] we turned our attention to the more complex problem of recreating catalytic metal sites. This is arguably a more ambitious goal, as the design of the metal binding site must not only include the primary coordinating ligands but support substrate access for efficient catalysis.

As a first attempt at inserting a catalytically active metal into our scaffolds, we targeted the symmetric tris(histidine) environment of carbonic anhydrase (CA). CA catalyzes the reversible hydration of CO_2, Reaction 1, and is critical to blood pH buffering and respiration. Native CA represented a good first target due to the relative simplicity of the metal binding environment as well as high catalytic activity.[17] Mutating two different leucine layers in the TRI scaffold at each end of the coiled-coil, one with cysteine near the N-terminus and the other with histidine near the C-terminus, gives TRIL9CL23H. Crystallographically, the tris(cysteine) site was shown to bind a Hg(II) ion, for structural stability; while the tris(histidine) site supported a zinc ion for catalysis.[12]

$$HCO_3^- + H^+ \rightleftharpoons CO_2 + H_2O \qquad \text{Reaction 1}$$

The inclusion of two layers of metal binding residues destabilized the structure compare to the parent TRI system, but the inclusion of the heavy metal binding site improved the stability beyond that of the nonmutated form. The structural site was shown to increase the stability of the 3SCC significantly through formation of a trigonal Hg(II)-Cys_3. Comparing crystal structures, the zinc active site was extremely similar geometry to that of native CA, including an exogenous water or hydroxide coordinated to the zinc, though orientation of the coordinating imidazoles differs between the two.(Figure 2)

We examined $[Hg(II)]_S[Zn(II)]_N$TRIL9CL23H for p-nitrophenyl acetate (pNPA) hydrolysis and CO_2 hydration activity. The hydrolysis of pNPA is well-studied due to the ease of monitoring the formation of the colored p-nitrophenolate. Our CA model $[Hg(II)]_S[Zn(II)]_N$TRIL9CL23H showed a pH dependence on activity (Figure 3, pKa of hydrolysis ~ 8.8), with the maximum k_{cat}/K_M within 100-fold of CAII (the isoform with the highest pNPA activity) at pH 9.5. Table 2 compares the activities of our model scaffolds for

pNPA hydrolysis. Notably, our CA mimic did not exhibit product inhibition under our conditions, a common issue with small molecule CA models.[18]

Significantly, this model lacks an important secondary sphere interaction which plays an important role in enhancing the rate of CO_2 hydration in CAII. T199A mutants of CAII remove a hydrogen bond acceptor that has been shown to activate the zinc-coordinated water in the mechanism of hydrolysis[19], reducing the activity approximately 100-fold vs. native enzyme, falling to comparable rates as our CA model. As our $[Hg(II)]_S[Zn(II)]_N$TRIL9CL23H only reproduced the primary coordination sphere, we had essentially mimicked the activity of CAII T199A.

When we examined the rate of CO_2 hydration activity, the native reaction of CAII, $[Hg(II)]_S[Zn(II)]_N$TRIL9CL23H showed rates within 500-fold of the native enzyme at pH 9.5, outperforming the best small molecule CA model by over 70-fold (Table 3). Since our report, models with higher pNPA activities have been described, such as MID1, which showed a maximum k_{cat}/K_M of 660 M^{-1} s^{-1} at pH 9.[20] To date, $[Hg(II)]_S[Zn(II)]_N$TRIL9CL23H retains the title of highest CO_2 hydration activity within a model. This paper was a keystone work, showing what could be achieved with our de novo scaffolds, by reproducing only the first coordination sphere alone.

2.2 Impact of zinc binding site position on hydrolytic activity

There is the potential that the presence of the second metal site Hg^{II}_S enhanced the activity of our CA model, by altering the fraying or “breathing” of the individual strands of the 3SCC. We therefore examined models that lack the stabilizing tris(cysteine) heavy metal binding site.[21] When the Cys layer was removed, TRIL23H denaturation studies demonstrated that the 3SCC was less stable, though the zinc affinity was unaffected. The activity of this model to pNPA was nearly identical to that of $[Hg(II)]_S[Zn(II)]_N$TRIL9CL23H except at high pH, which we attributed to decreased stability caused by the loss of the stabilizing Hg(II)S site under more basic conditions.

To determine whether the specific location of the metal binding site plays a significant role in the resulting activity, we next designed CA models that modified the position of the zinc site within the leucine layered core of our 3SCC design. For example, the orientation of the coordinating histidine residues, and the resulting placement of the zinc ion has the potential to significantly influence both solvent and substrate access, as well as hydrogen bonding interactions; factors known to play significant roles in the activity of native CAs.[22] Our scaffolds offer a significant advantage to designing metal binding into native or more complex scaffolds as the inclusion of the metal binding site a) does not significantly alter the scaffold geometry, b) can be moved to different positions in the 3SCC by simply changing the location of leucine substitutions, c) can be placed in a number of approximately geometrically equivalent positions along the 3SCC due to the presence of multiple leucine layers.

We developed the flipped complement to $[Hg(II)]_S[Zn(II)]_N$TRIL9CL23H, $[Hg(II)]_S[Zn(II)]_N$TRIL9HL23C, placing the zinc active site towards the N-terminus.[21] This construct has 10-fold lower zinc affinity than TRIL9CL23H and TRIWL23H at pH 7.5

and 4-fold weaker at pH 9 highlighting the importance of metal site position and orientation in *de novo* scaffolds. Analysis of pNPA hydrolysis kinetics under Michaelis-Menton conditions showed the flipped construct had a reduced value for k_{cat} of 0.020 s^{-1} at pH 9.5 (half that of TRIL9CL23H). This decrease in k_{cat} was, in part, counteracted by tighter a tighter K_M so k_{cat}/K_M only reduced from 23.3 $M^{-1}s^{-1}$ to 15.8 $M^{-1}s^{-1}$ (Table 2). Earlier, we had shown that the position of the heavy metal binding tris(thiolate) site possessed different properties if it were placed in the *a*-site position vs a *d*-site within the heptad; for example, the pKa, coordination number, and ligand positions change for cadmium and mercury in these sites.[23] Hypothesizing a similar effect could exist for zinc in tris(histidine) sites, TRIWL9CL19H was studied. This construct showed a 5-fold decreased affinity for zinc and an increased pKa of pNPA hydrolysis to 9.6 from 9.2 in TRIL9CL23H (Figure 3). The construct also showed good pNPA hydrolysis rates with k_{cat}/K_M values similar to TRIL9CL23H and TRIL9HL23C, but with an increase of the K_M to 2.8 mM. These results demonstrate the potential to tune the K_M and pKa using metal binding site repositioning, but the catalysis is largely unaffected and metal site location in a *de novo* designed scaffold should be based off ease of incorporating secondary sphere interactions that enhance the rate.

2.3 Development of a zinc hydrolytic 3HB protein

The intrinsic symmetry of our self-assembling 3SCC scaffold has numerous benefits, as already discussed. However, in order to design functional hydrogen bonding network and to model the asymmetry in the second coordination sphere of CAII (*vida supra*), we next designed a model of CA in our α_3D type scaffold.[24] Replacement of three of the core leucine layers towards the C-terminal region of the original α_3D, along with a H72V mutation to remove possible unintended zinc coordination gave α_3DH3. Zinc binds tighter to this three helix bundle peptide than any 3SCC model, with apparent K_d = 0.15 μM and 0.06 μM at pH 7.5 and 9, respectively (TRIL9CL23H K_d = 0.8 μM and 0.22 μM at pH 7 and 9). Using extended X-ray absorption fluorescence spectroscopy, the zinc coordination sphere was fit to 3 zinc histidine scatterers at 1.99 Å and one zinc-oxygen scatterer at 1.90 Å, which are nearly identical parameters to those of the native CAII.

As with the TRI 3SCC, α_3DH3 showed a pH dependence on CO_2 hydration activities. The reaction was analyzed between pH 8 and 9.5, and fit for a maximal efficiency at higher pH, (k_{cat}/K_M) 69,000 $M^{-1}s^{-1}$. The catalytic pKa was 9.4, compared to 8.8 for the 3SCC model. The maximum measured k_{cat}/K_M was 38,000 M-1s-1, 14-faster than the best small molecule model, but 2.5 times slower than the best TRI 3SCC model, TRIL9CL23H. Again, this model did not display any product inhibition, a significant advantage over small molecule studies to date. Compared to the native enzyme, α_3DH3 falls within 1400-fold of the fastest isozyme, CAII (Table 3).

2.4 Zinc catalyzed hydrolytic activity in other helical scaffolds

As mentioned above, other research groups have developed different helical scaffolds that bind zinc ions and have been shown to possess zinc catalyzed hydrolytic activity. The Kuhlman group developed a zinc-mediated homodimer in a helix-turn-helix motif. The design of the homodimer contains two four coordinate zinc ions, supported by a His_3O

binding site. A fourth His ligand (intended as a fourth primary coordinating ligand) creates a small molecule binding pocket. As with our current generation of CA models, no second sphere interactions were intentionally designed. MID1-Zn showed improved hydrolysis of pNPA as compared to our TRI scaffold, with a k_{cat}/K_M of 660 $M^{-1}s^{-1}$ at pH 9, attributed to the more accessible active site cleft in the homodimer. Recently, this group has described the artificial evolution of the MID1 catalyst, improving upon the hydrolysis of a racemic fluorogenic ester 70,000-fold.[31] A designed metallo-β-lactamase was described by the Tezcan group consisting of a tetramer of modified cytochrome cb562, Zn_8:$AB3_4$[32]. The design of this scaffold relies on a zinc mediated self-assembling interface, such that four of the eight zinc function in a purely structural role, with the remaining four being catalytically active. This protein, in addition to conferring the metallo-β-lactamase activity, also showed good activity towards pNPA as well, with k_{cat}/K_M of 32 $M^{-1}s^{-1}$ at pH 9. In a similar approach, the Korendovych group showed how short peptides could self assemble, facilitated by zinc binding to His residues, to form zinc mediated amyloid fibrils with esterase activity.[33] These zinc binding amyloid fibrils, which consist of beta-sheet structure, rather than alpha helices, can catalyze ester hydrolysis, with a k_{cat}/K_M of ~150 $M^{-1}s^{-1}$ at pH 9 and a maximal k_{cat}/K_M 360 $M^{-1}s^{-1}$ at pH 10.3.

3. Development of copper centers as models of nitrite reductase activity

The *de novo* design of redox active metalloenzymes is more complicated than that of redox inactive metal centers, such as the zinc-containing models of CA. The change in the oxidation state of the metal will not only modify the overall electrostatic charge of the binding site, but, generally speaking, different oxidation states possess differing ligand environment and geometric preferences. Cu^{I}, for example, will show stronger preference for softer ligands and lower coordination number than Cu^{II}. Therefore, the *de novo* design of redox active metalloenzymes must consider the coordination environment of both the reduced and oxidized species, in addition to those criteria described above for redox inactive metals. Fortuitously, our *de novo* scaffolds offer some significant advantages over small molecule models, as the geometry of the metal binding site is constrained by the stable folding of the scaffold in the absence of metal. Additionally, only small reorganizations have been observed upon metal binding to our scaffolds, dependent on the location of the site within the scaffold and on the metal being examined.[34] And, as mentioned above, most of the current small molecule mimics are only soluble in organic solvents and are optimized to only bind a single copper oxidation state. Thus, our scaffolds are well suited to model metalloenzymes that undergo redox activity.

Recently, we have described several advances in our development of copper nitrite reductase activity (CuNiR). CuNiRs catalyze the reduction of nitrite to nitric oxide via Reaction 2, the second step in the dissimilatory pathway of nitrate to dinitrogen. CuNiR is a homotrimeric copper enzyme that possesses two copper binding sites, a type 1 copper electron transfer center $Cu(His_2)(Cys)(Met)$, and a type 2 catalytic copper center $Cu(His_3)(OH_2)$. The catalytic type 2 copper exists in a distorted tetrahedral environment, intermediate to the preference of the cuprous and cupric species in order to minimize the reorganization energy of the protein on changes in oxidation state.[35] The mechanism of nitrite reduction is well studied, briefly, nitrite binds to the type 2 catalytic site first, followed by gated electron

transfer from the reduced type 1 site to the type 2 site. Proton-coupled electron transfer, facilitated by hydrogen bonding between a histidine (H225) and an aspartate (E98) to water and the bound substrate, facilitate the catalysis.[36] These residues have been shown to be critical for the high activity of native CuNiR with at least 100-fold decrease in activity upon their removal.

$$NO_2^- + e^- + 2H^+ \rightleftharpoons NO_2 + H_2O \qquad \text{Reaction 2}$$

3.1 First generation CuNiR models

Noting the geometry of the zinc site in our CA model $Hg^{II}_{S}Zn^{II}_{N}(TRIL9CL23H)_3$ was very similar to that of the type 2 Cu in CuNiR, we first looked at copper bound in the tris(histidine) site of TRI 3SCC environment using the simplified TRIL23H which omits the heavy metal binding tris(cysteine) site.[37] Overlay of the zinc site in $Hg^{II}_{S}Zn^{II}_{N}(TRIL9CL23H)_3$ with copper centers of CuNiRs showed similar ligand geometries, each coordinating the metal with the ε-nitrogen of the histidine and a coordinated water ligand (Figure 4). The charge and Lewis acidity of Zn(II) resembles that of Cu(II), and the d^{10} electron configuration mimics Cu(I). Therefore, we were confident that this peptide would be a suitable model of CuNiR type 2 site, allowing study of the reaction in aqueous environment using the native ligands, unlike small molecule models, while removing the convolution of the two copper sites in the native CuNiR.

Cu(I) binding to the histidine sites was confirmed using ^{1}H-NMR.[37] The metal free apo-TRIL23H showed two singlet peaks in the aromatic region of the ^{1}H-NMR, at ~7.7 and 7.0 ppm corresponding to the ε- and δ-nitrogen, respectively. Upon addition of 1 eq of Cu(I), these singlets gave rise to multiple peaks, indicating copper binding specifically to the histidine residues. Additionally, pH titrations of the Cu-TRIL23H monitored using ^{1}H-NMR showed the presence of free imidazole protons only below pH 4.45, consistent with $Cu^{I}(His_3)$. Further characterization using XAS revealed that the 1s→4p pre-edge feature, the intensity of which can be diagnostic of cuprous coordination number,[38] was also consistent with a three-coordinate Cu(I). The extended X-ray absorption fine structure (EXAFS) of Cu(I)TRIL23H was best fit by 3 N/O scatterers at 1.93 Å with additional backscattering at longer distances characteristic of histidine coordination. The unusually large Debye-Waller factors of these His scatterers suggested distorted trigonal planar geometry. The Cu(I) K_d was determined to be 3.1 pM and 0.2 pM at pH 5.9 and 7.5, respectively, using competitive titration with bathocuproinedisulfonate (BCS^{2-}).

Cu(II) binding was investigated with visible absorption spectroscopy, with a broad absorption around 640 nm (ε = 135 M^{-1} cm^{-1}), consistent with a $Cu(II)(His)_3$ site containing either one or two exogenous water ligands.[39] The EPR spectra of Cu(II)TRIL23H was consistent with a five-coordinate type 2 copper $[Cu(II)(His)_3(H_2O)_2]$. Addition of nitrite to Cu(II)TRIL23H showed a 9 gauss decrease in the $A_{\parallel}$ indicative of nitrite binding to the copper center directly as previously shown for native NiR.[40] The Cu(II) K_d of this model was determined by quenching of Trp fluorescence to be 40 nM and 8.7 nM at pH 5.9 and 7.5, respectively.

It is possible to calculate the reduction potential of the Cu(I)/Cu(II) couple using the Nernst equation using affinities for Cu(I) and Cu(II). The reduction potential for this model is 400 mV at pH 5.9 and 430 mV at pH 7.5, much higher than is typical of type 2 copper centers,[41] and actually falling closer to those reported for type 1 copper centers. This could be due to the trigonal geometry of the Cu(I) state being stabilized in the highly symmetric $(His)_3$ binding site, raising the reduction potential. Despite this elevated reduction potential, we examined the NiR activity of CuTRIL23H. This model was shown to be capable of generating NO from nitrite, by capture of the produced NO to form the colored FeEDTA(NO).[42] Headspace FTIR-GC analysis showed no detectable amounts of N_2O formation, which is a common byproduct in other NiR model systems, and represents a significant success in our *de novo* approach.

Using ascorbate as a sacrificial electron donor, whose UV signal can be conveniently followed at 265 nm to monitor the reaction, we assayed for NiR activity under catalytic conditions and determined a maximum first-order rate constant of 4.6×10^{-4} s^{-1} at pH 5.8. A significant decrease in the reaction rate as a function of increasing pH is likely caused by changes in the $Cu(I)His_3$ coordination environment or the involvement of the protons in the nitrite reduction reaction. Though this catalytic rate represents only a modest rate compared to that of native CuNiR's, this model was the only example of a stable, functional $Cu(His)_3$ site in aqueous solution capable of multiple turnovers with no observed decrease in efficiency.

3.2 Probing the Cu site

It is exceptional that our first generation *de novo* enzymes possess good activities in the absence of any modelling beyond that of the primary metal coordination sphere. Thus, to improve on the CuNiR activity, we understood that optimization would largely depend on the effect of modifications to the second coordination sphere as well as the electrostatic environment surrounding the cooper binding site.[43] Changes to the reaction's free energy barrier (ΔG‡), resulting in modification to enzymatic rates, can be brought about by changes to the electrostatic environment of the active site, through stabilization of charge density in the transition state. Dynamic aspects of enzyme active sites, that is the pico to microsecond or longer vibrational and translational motion inside and around the catalytic site, are also involved in determining overall reaction rates. The dynamics and electrostatic factors that drive catalysis can be studied using vibrational probes of enzyme active sites.[44] These studies provide details on active site flexibility, which determines how substrate accesses the active site and product is transported away, and changes of reaction barrier with respect to the molecular dynamics around the active.[45]

We studied the copper environment within our CuNiR model, in collaboration with the Kubarych group, by examining the ultrafast dynamics of carbon monoxide bound to CuTRI-H as a vibrational probe of the $Cu(His)_3$ environment.[46] We used two-dimensional IR spectroscopy as an *in situ* probe of the active site to further connect our understanding between our *de novo* constructs and small molecule models.[47] The 2D-IR spectrum showed two bands that correspond to the excitation of the ground state ($\nu = 0$ to 1, 2063 cm^{-1}) and excitation of the first excited-state ($\nu = 1$ to 2, red-shifted to 2039 cm^{-1} due to CO

vibrational anharmoncity) transitions. Following vibrational excitation, we observed a time-dependent anharmonicity in the vibrational modes of the bound CO, with a decay constant of 2 ps. The frequency shift brings the two bands closer together, the ν_{01} transition redshifts and the ν_{12} transition blueshifts. The magnitude of the excited-state blueshift exceeded that of the ground state redshift. We also investigated the modified peptide (TRI-H K22Q K24Q), which replaces six positively charged lysine residues near the copper site with neutral glutamine. This protein exhibited similar anharmonicity to the vibrational transition, suggesting that this feature is reproducible in other sequences and is likely common to our other 3SCC scaffolds.

Computer modelling calculations on the full *de novo* protein were performed to understand the steric and electrostatic interactions that give rise to this behavior. Using a QM/MM ONIOM approach, with the Cu, imidazole ligands, and CO adduct in the QM (B3LYP/6–311G(d,p)) layer, we observed a >6° decrease in Cu-C-O bond angle for the vibrational excited state. This bend is consistent with the picosecond dynamics observed in the vibrational frequency shifting dynamics and supports that the peptide enhances coupling to the CO stretch, highlighting the role of the peptidic environment, and one of the significant advantages to our *de novo* approach. Further calculations showed that the electric field from the parallel 3SSC peptide scaffold distorts the geometry of the copper-coordinating histidine ligands and is responsible for the Cu-C-O bend coupling to the CO excited state stretch, rather than directly affecting the carbonyl. This excited state bend coupling was strongly dependent on the orientation of histidine coordination to the copper center, likely a result of the position of the dipole moments (~3.6 D) from each of the individual His ligands (Figure 5). These calculations reveal the role of electrostatics in tuning the molecular dynamics and the energy landscape of ligand coordination within our $Cu(His)_3$ site. Thus, by modification of the electrostatic environment, either by changing the location within the 3SCC (coiled coil dipole), or by positioning of charged residues in proximity to the site it is possible to improve our CuNiR.

To improve on this modest CuNiR activity, we then considered the role of the electrostatic environment surrounding the copper binding site first by modification of outer-sphere residues that change the electrostatic environment of the copper center (Figure 6A), followed by changes to the inner-sphere residues (Figure 6B).

3.3 Modification to charge density around the copper binding site

Modification of the charge density around a redox active metal binding site (by substituting residues of different charges) will have significant effects on the stability and structure of the different oxidation states, and thus the redox potential, and ultimately the catalytic efficiency or mechanism of redox active metalloenzyme sites.[48] For example, the protein peptidylglycine α-hydroxylating monooxygenase (PHM) has a (His_3) active site structurally similar to CuNiR, but plays a role in electron transfer instead of being directly involved in catalysis as is the case for CuNiR.[49] Historically, these studies were performed on native proteins, which bring along the complexity and convoluting factors of native systems. Therefore, we sought to examine the role of the electrostatic environment around the Cu-center in our *de novo* CuNiR 3SCC model TRI-H, by modifying the charge of nearby

residues. We designed and synthesized several modified peptides that substituted residues located neither within the hydrophobic interior of the 3SCC (which could lead to significant destabilization) nor directly involved in Cu-coordination listed in Table 4 (upper) and shown in Figure 6A.[50]

The pH effect on copper binding to the outer sphere modified peptides was followed using UV visible absorption spectroscopy. Near neutral pH, Cu^{II}-TRI-H shows a broad band centered 644 nm, assigned as the d-d transition of the copper in the His_3 environment. The pH profiles of copper binding to TRI-H are complicated by multiple competing and overlapping processes that occur as a function of pH. The most significant of which, the formation of 3SCC, is known to occur around the pKa of glutamate residues involved in salt bridging in *e*-sites, around pH 4.5, the protonation state, charge and copper binding propensity of the imidazole ligand (pH 5.5 – 8), and the protonation state of any coordinated water (pH >8). Thus, there are two major changes to the UV-visible absorption spectrum as a function of pH: a low pH transition associated with 3SCC formation and copper binding to the $(His)_3$ site, complete by approximately pH 5; and the deprotonation of the water coordinated to the copper, forming hydroxide with a pKa ~8.5 (Figure 7). Other outer sphere modifications with different charges showed similar pH profiles for the lower pH copper binding, but distinctly different profiles for the higher pH effects due to the various pH effects at play. TRI-EH, for example, showed a significantly more basic water deprotonation step (pKa 9.86). XAS measurements of the cuprous and EPR of the cupric forms of TRI-H and TRI-EH showed no significant difference in the geometry of the copper site between the two scaffolds, at pH 5.8. Minor differences in the intensity of the Cu(I) pre-edge feature and lower Debye-Waller values in the values of Cu-N scatterers in the EXAFS region, suggest a slightly more symmetric trigonal planar geometry for the TRI-EH vs. a more distorted T-shaped geometry for the parent TRI-H.

Dissociation constants for the Cu(I) and Cu(II) states of the models were measured for the series of outer sphere modifications. The Cu(I) K_d was found to decrease by over two orders of magnitude as the charge was decreased from 0 to −12, while the K_d of the Cu(II) only showed a modest decrease in affinity for the same modifications. These values were then used to calculate reduction potentials, using the Nernst equation, and plotted as a function of the charge difference from the parent TRI-H (Figure 8A) at two specified pH values. These also show a linear decrease as a function of increasing negative charge at both pH 5.8 and 7.5 with a slope of 100 mV per 1.6 pH units, consistent with one proton per electron. This decrease in the calculated reduction potential is more reflective of the destabilization of the cuprous species in more negatively charged environment than the stabilization of the cupric form, resulting in a less positive reduction potential. The differences in the affinities of the cupric and cuprous forms of each model are separated by approximately 100 mV, with the more acidic pH having the more positive reduction potential.

We had originally designed the series of outer sphere CuNiR models with increasing negative charge to stabilize the more positively charged Cu(II) species which would, in turn, decrease the reduction potentials. While we did indeed observe the expected decrease in reduction potential across the series, it was due to the destabilization of the Cu(I) rather than the stabilization of the Cu(II). Thus, because the Cu(I) affinity increased going from more

negative to more positive charged metal binding environment, this suggested the involvement of H-bonding and salt-bridging interactions. Briefly, we proposed a rack-induced binding environment, similar to that suggested for blue copper electron transfer proteins.[51] In this model, the protein matrix constrains the metal coordination environment, leading to changes of the stability of the different oxidation states that are exploited to tune the redox-potential of the copper center. Our results suggest that, in our model CuNiR, this induced-rack effect is greater for the Cu(I) oxidation state. Specifically we proposed a hydrogen bonding interaction between Glu22 and His23 that orients the imidazole ligand.

Finally, we examined the series of outer sphere modifications for CuNiR rates, using the ascorbate assay described above. As the charge was decreased from 0 to −12, we observed a 4-fold increase across the series in NiR activity and a correlation with reduction potential (Figure 8B). At pH 5.8 for our outer sphere models, the higher the reduction potential, the lower the rate. Though this appears to show a linear trend linking the rate to the reduction potential, the assay conditions, in which ascorbate is added in significant excess, invalidate the conclusion this is due to electron transfer rates, as we have shown that the reduction of Cu(II) to Cu(I) by ascorbate is not rate-limiting. Instead, we suggest that the reorganization energy upon oxidation (Cu^{I} trigonal to Cu^{II} pseudotetrahedral) limits the observed rate. This study established that changes to the charge environment around the active site, through residue substitutions in positions nearby, can be used to modify properties that influence the reduction potentials, and NiR activities in a systematic fashion.

3.4 Modification to steric bulk and adding potential hydrogen bonding residues to the inner sphere

Having established the influence of outer sphere modifications on CuNiR activity, we then turned to examining the role of inner sphere modifications. It is well known that inner sphere residues of an enzyme play significant roles in catalysis, and mutations of inner sphere residues has been shown to significantly alter catalytic rates and efficiencies. Therefore, using our rational design strategy, we identified two positions in the 3SCC where substitution of the Leu layer for other residues (Figure 6B) could lead to modification of the coordination environment of the bound Cu or Cu-coordinated water(s). We had previously shown that we could control the coordination number of Cd bound to tris(cysteine) sites by modifying the sterics of the hydrophobic layer spacing in the core above or below the $Cd(S_3)$ binding site).[16, 52] Thus, by modification of the sterics around a catalytically active metal binding site, we should be able to tune the substrate and solvent access.

Using this approach with our $Cu(His_3)$ NiR site, we substituted leucine residues in position 19 and 26, the leucine layers directly above and below the Cu(NiR) site (Table 4 and Figure 6B).[53] We increased the steric bulk above the Cu binding site by substitution with isoleucine or D-leucine, as our first-generations CuNiR model was thought to be five-coordinate in the cupric state (compared to four-coordinate for native CuNiR), and believed that increasing the bulk above the metal binding site would decrease solvent access and lower total Cu-coordination number. We then tested the effect of decreased steric bulk above or below by substitution with alanine, as crystal structures of our heavy metal binding scaffolds have shown that decreased steric bulk can permit up to four additional water

molecules.[34] Finally, in order to study the effect of hydrogen bonding to the Cu-coordinated water(s) or histidine imidazole ligands and/or the addition of extra Cu-coordinating residues, we made scaffolds that positioned aspartate above and below the copper site.

We examined this series of CuNiR models for CuNiR activity and observed rate constants that split the series into two identifiable groups (Figure 9, green bars) – those whose CuNiR initial rate constants were approximately the same as the parent TRI-H (L19I and $L19_DL$), and those whose CuNiR rate was between 60- to 75-fold greater (Ala and Asp substitutions). We believed that this trend in rate differences between the two groups was due to structural differences in the resting state of the Cu(I) forms, as we have shown that the reduction of the Cu(II) is extremely rapid under our assay conditions. Therefore, we collected X-ray absorption data and compared the 1s → 4p energies in the XANES region (Figure 10) and bond distances from EXAFS.

The increase in intensity of the Cu(I) pre-edge, as well as increases in copper ligand bond distances from EXAFS upon decreasing the steric bulk around the binding site suggests that rather than permitting extra coordinating ligands to bind to the copper site, the reduction in steric bulk allows the Cu(I) state to relax and reduce coordination number from 3 to 2. This was the opposite of what we had observed when we modified sterics surrounding heavy metal binding sites, where decreased sterics led to an increase in coordination number. We observed that the XANES 1s → 4p energies could accurately define the two groups, with the more active constructs showing a shift to higher energy compared to the parent TRI-H, and those whose rates were approximately the same showing a similar energy. This energy shift, which provides information on the electron density around the copper site and thus its ability to participate in redox chemistry, appears to correlate with the increase in NiR activity, and would also impact the potential energy landscape of the transition state during catalysis (*vida supra*). Native CuNiR have a four-coordinate $Cu(His)_3(H_2O)$ in both the oxidized and reduced state, suggesting that the reorganization of our model copper binding sites may be a limiting factor in our activity enhancements.

3.5 Role of histidine coordination isomers in CuNiR activity

Another significant feature of imidazole moieties is the potential for either of the imidazole nitrogens to be the coordinating ligand. Returning to our discussion on PHM and CuNiR, these two enzymes display vastly different copper chemistries, yet possess the same Cu(His)3 copper environment. Close inspection of the structures of CuNiR (PDB: 4YSE[54]) and PHM (PDB: 1PHM[55]) reveals different tautomeric coordinative isomers between the Cu and His, with the former coordinating copper through the N_ε and the later through N_δ of the imidazole. The difference in coordination, N_ε vs. N_δ, has been shown to be common in T1 Cu electron transfer sites vs T2 Cu catalytic sites. In order to determine the orientation of the histidine coordination in our CuNiR model, TRI-H, we designed scaffolds that included N-methylated histidine as the primary coordinating ligands (sequences in Table 4).[56] Thus, we could compare N_ε-methylhistidine (TRI-$_{\varepsilon m}$H, N_δ free to coordinate copper) with N_δ-methylhistidine (TRI-$_{\delta m}$H, Nε coordinating) to our original design and tease out not only the coordination state, but also the effect of forcing the flipped coordination mode, to

determine directly the influence on copper-histidine coordination isomers on properties of our well understood metalloezymatic system.

It is important to note here that methylation of the imidazole fundamentally alters properties of the ligand, not limited to only the N-coordination. The replacement of one of the NH with N-meth, removes an opportunity for H-bonding, and changes the pKa and accessible charge of the ligand. Also, the methyl group is much more electron donating, changing the electronic nature of the imidazole ligand, in ways that are often difficult to predict.[57] Finally, N-methyl imidazoles are much more sterically demanding than the parent histidine groups, which could significantly impact the geometry and stability of our Cu sites. Thus, there are numerous factors that are at play when considering N-methyl histidine substitution.

We characterized the effect on forced ε- or δ-nitrogen coordination (by methylation of the other imidazole nitrogen) on the geometry of the copper binding site, redox potential, and catalytic activity. EPR, XAS, and UV visible absorption spectroscopic data suggested that TRI-$_{\varepsilon m}$H has a lower number of coordinating imidazoles than TRI-$_{\delta m}$H for both the Cu(I) and Cu(II) states (Figure 11). Significantly, TRI-$_{\delta m}$H more closely mimicked the geometric features of the original TRI-H, with TRI-$_{\varepsilon m}$H showing more of a tetrahedral nature for the Cu(II) species (N_3O vs. N_2O_2 coordination environment for TRI-H and TRI-$_{\delta m}$H) and more two-coordinate character for Cu(I). vs. three-coordinate for the other two. These data suggest that the parent TRI-H coordinates with the ε-nitrogen. As with our inner sphere modifications, we observed a shift in the 1s → 4p energy in the XANES region, with the TRI-$_{\delta m}$H matching the energy of the parent, while TRI-$_{\varepsilon m}$H is slightly higher energy (Figure 10B).

Finally, we compared the NiR activity of the N-methyl histidine containing scaffolds to our previous designs (Figure 9, magenta bars). We observed the largest increase in NiR activity through modification of the primary coordinating ligands. Interestingly, the larger enhancement in rate came from methylation of the δ-nitrogen, forcing ε-nitrogen coordination, the same as in TRI-H. We concluded that an inductive-like effect upon N-alkylation, linked to HOMO energy increases from more electron-rich ligands, accounted for the difference between the two scaffolds. We attempted to combine the features that generated the best NiR activities from the previous inner sphere modifications (reduction of steric bulk through L19A mutation, 75-fold increase in rate vs. TRI-H) with the best primary coordinating substitution (TRI-$_{\delta m}$H, 260-fold rate enhancement), to give TRI-$_{\delta m}$H L19A. Though this only resulted in a modest 2.5-fold increase in rate vs. the TRI-$_{\delta m}$H, this scaffold is the best CuNiR model in a homogenous aqueous system to date, with 640-fold rate enhancement vs. our first generation CuNiR, TRI-H. Though this is currently the best synthetic homogenous copper catalyst for CuNiR activity, the rate falls 400,000-fold short of the native system.

Michaelis-Menten kinetics analysis of our CuNiR activities revealed that this decreased activity is due to factors that impact both the maximal catalytic rate as well as substrate access and binding (Table 5). V_{max} plateaus, while the biggest effect on catalytic efficiency is due to K_M effects. Again, we have thus far not included the critical acid-base catalyst, an aspartate that is important in the activity of the native protein, in our CuNiR models. We

have already attempted to add a nearby Asp residue, but the enforced three-fold symmetry meant that three Asp residues were positioned near the $CuHis_3$ site, and we believe that those aspartate residues interacted with each other rather than with the Cu site.[53] Additionally, we observed a significantly decreased K_M as compared to small molecule models, suggesting that substrate recognition and access is limited in our scaffold design. This difference may also reflect NO_2^- binding to Cu(I) vs Cu(II). This suggests we need to make future alterations that enhance substrate binding, such as new scaffolds that will allow for asymmetric modification of the scaffold. We have developed such a scaffold which will be described soon.[63]

4. Design of electron transfer sites in de novo scaffolds

We now turn to discussion of our recent developments in the *de novo* design of electron transfer sites in our alpha helical scaffold systems. Metal binding sites that transfer electrons, either across membranes, between metal binding sites, or coupled to proton transfers have to have metal binding sites that can support the different geometric and ligand preferences of the different redox states, as is the case for metal binding sites involved in redox cycling in a catalytic site, such as CuNiR. As discussed in more detail above, this requires careful consideration of the coordination number and geometry, and therefore, ligand positioning within the scaffold. We will highlight the development of our models for iron-containing rubredoxins and copper containing cupredoxins.

4.1 Development of non-heme iron rubredoxin models

FeS cluster proteins are a class of proteins with cofactors of varying complexity from a single Fe bound by 4 cysteines (rubredoxin)[64] to multi-atom cofactors that must be assembled by separate protein machinery before being inserted into the final target protein (the P cluster of nitrogenase).[65] The relative simplicity of rubredoxin and the extensive literature available on its geometry and spectroscopy make an attractive target for metalloprotein design.[3b]

Previous rubredoxin design attempts focused on recapitulating the hairpinof the native binding site showing that the same secondary structure and metal binding site could be created using a *de novo* protein sequence.[66] Ferinas and Regan used the program Metal Search to put a tetrahedral Cys_4 site into the B1 domain of IgG-binding protein G, but while this construct was able to recapitulate the Fe(III) spectroscopy of rubredoxin it was not a functional redox center.[66d] Nanda and DeGrado created a rubredoxin mimic by recapitulating the local secondary geometry around the Fe in the native protein and minimizing the surrounding protein needed to maintain this geometry 40 amino acid peptide.[66b] This construct not only successfully mimicked the Fe(III) spectroscopy of native rubredoxin, but was the first *de novo* rubredoxin mimic capable of reliable redox cycling up to 16 cycles. Arguably the most successful simplification of the rubredoxin fold was created by Jacques and Sénèque within a 18 amino acid peptide composed of a cyclic portion and a linear tail.[66a] While this construct was capable of less redox cycles than the Nanda and DeGrado model (7 compared to 16) it successfully recreated the Fe(II) and Fe(III) spectroscopy of native rubredoxin with less than half of the amino acids.

We focused our efforts on determining whether this hairpin turn secondary structure was necessary to recapitulate the spectroscopy of a rubredoxin by implanting a rubredoxin-type Cys_4 binding site within an alpha helical bundle scaffold.[67] Our lab had previously designed two Cys_4 proteins based on the heavy metal binding Cys_3 peptide α_3DIV (α_3DIV H72C or L21C) as models for the Cd binding site of CadC.[68] Using ^{113}Cd NMR we determined that the H72C variant which positioned the fourth Cys in a nearby loop region formed CdS_3O while L21C, which positioned the fourth Cys as part of a CXXC chelate motif, formed CdS_4. We tested both α_3DIV H72C and L21C as prospective rubredoxin models.

When expressing α_3DIV H72C and L21C in media containing supplemental Fe the lysate of the L21C variant was red in color indicating some level of Fe incorporation *in vivo*. Similar expressions of either α_3DIV alone or its H72C variant were a standard yellowish color and so our characterization efforts focused on α_3DIV L21C as a possible rubredoxin mimic using UV-visible absorption, Mössbauer, EPR, Magnetic Circular Dichroism (MCD), and X-ray absorption spectroscopies. Purified peptide was reconstituted with Fe by addition of Fe(II) before oxidizing in air to produce the Fe(III) form. Optical absorption spectra of Fe(III)-α_3DIV L21C had LMCT peaks at similar energies as native rubredoxin but with about ~30% of the expected intensity, consistent with other spectroscopies that would indicate some proportion of contaminant within the construct (*vida infra*).[69]

Using MCD analysis, the optical spectrum of Fe(III)-α_3DIV L21C was deconvoluted to nine unique peaks matching in energy to those seen in native rubredoxin. Further investigation of the optical spectrum through variable temperature variable field MCD determined saturation behavior that was consistent with native rubredoxin. 4.2K Mössbauer spectra of Fe(II)-α_3DIV L21C were consistent with those of native rubredoxin but high field spectra revealed two unique components: 60% FeS_4 and 40% FeS_3O.[70a] The Fe(III)-α_3DIV L21C Mössbauer results produced similar results with the bulk of the sample having similar spectra as rubredoxin but 25% of the sample was concluded to be impurities of ferric oxides/hydroxides. This impurity was also observed in the X-band EPR spectrum though it was largely consistent with native rubredoxin. Lastly, EXAFS analysis revealed that Fe(II)-α_3DIV L21C was dominated by a single Fe-S bond at 2.32 Å.

We analyzed the electrochemistry of Fe(II/III)-α_3DIV L21C to investigate its activity as an ET site and determined a one-electron transfer with a potential of −75 mV which falls within the −90 to 50 mV range seen in native rubredoxins.[64a, 64f, 70b, 71] pH dependent studies of the redox potential found it was a 2-proton, 1-electron proton coupled event. This differs from native rubredoxins whose redox potentials show no change with pH. We hypothesize that charged residues near the metal binding site of our construct may be the cause of this effect. Chemical reduction with dithionite followed by air oxidation could be cycled up to three cycles before the construct was irreversibly bleached, likely caused by cysteine oxidation.

This characterization effort was the most robust ever undertaken for a designed rubredoxin and showed that one can construct a tetrahedral FeS_4 center within a rigid scaffold unrelated to the native secondary structure. We also determined that the CXXC motif of native

rubredoxins is an important part of maintaining this metal binding geometry within a protein as our scaffold without this motif was unable to recapitulate the spectroscopy of a tetrahedral FeS_4. Comparison of MCD with Mössbauer and EPR showed that our construct also reaffirms the D sign controversy seen in native rubredoxins in which MCD favors a negative value while Mössbauer and EPR favor a positive value.[70a, 72] Moving forward, high-field EPR and further protein design of this construct can be used to investigate this apparent disagreement.

4.2 Development of cupredoxin models

Type 1 (T1) Cu proteins are electron transfer proteins with a Greek beta barrel fold and a $CuHis_2CysXxx$ binding site in which Xxx can vary between Met, Gln, and (in one instance) Glu. These proteins have long fascinated the bioinorganic community because of their constrained geometry, unique optical spectroscopy leading to bright blue, green, or red solutions, and compressed hyperfine coupling constant within EPR.[73] Blue T1 Cu proteins have an intense LMCT at 600nm assigned as a Cys-Cu π-$d_{x^2-y^2}$ transition, short Cu-Cys bond at 2.1–2.2 Å, and compressed $A_\parallel$ below 100×10^{-4} cm^{-1}.[74] Green T1 Cu proteins have an additional LMCT band at 450nm assigned as a Cys-Cu σ-$d_{x^2-y^2}$ transition with a ratio between the two intensities of around one, a not as short Cu-Cys bond at 2.2 Å, and similarly compressed $A_\parallel$.[75] Finally, red T1 Cu proteins have a much more intense σ LMCT at 390, blue-shifted and diminished Cys-Cu π-$d_{x^2-y^2}$ transition at 500nm with a ratio of ~3, T2 Cu protein-like EPR and Cu-Cys distance closer to 2.3 Å.[76]

Previous efforts to design T1 Cu proteins into unrelated scaffolds have largely produced green copper proteins.[77] Lu and Valentine showed that they could recreate the spectroscopy of a green copper protein with a H80C variant of Cu/Zn superoxide dismutase while Hellinga created a series of thioredoxin variants capable of recreating green copper spectroscopy upon the addition of the exogenous ligand azide.[77a, 77b] Using a combinatorial approach, Schnepf and Hildebrandt created and screened 180 different His_2Cys containing four helical bundle peptides and found several that had green copper protein spectroscopy.[77c] The most successful work towards a *de novo* blue copper protein was that of Shiga and Tanaka who modified a previous His_2Glu Cu binding protein within a four helical bundle scaffold to make a His_2Cys and successfully made a green copper protein using rational design.[77d] This construct could then be tuned to a blue copper protein by the addition of several exogenous ligands such as chloride, sulfate, acetate, and phosphate.[78] While all of this work was impressive and pushed the field forward, the need of an exogenous ligand to recapitulate the spectroscopy of a blue copper protein meant how one could design a self-contained blue copper protein in a *de novo* scaffold remained unanswered.

We had previously shown that a His_3 or Cys_3 metal binding site could be designed into the 3HB protein α_3D, but this was our first attempt at a mixed coordination sphere.[24, 80] Four different prospective cupredoxins were designed into the α_3D scaffold: CR1, CH3, CH4, and ChC2.[79] α_3DCR1 incorporates a His2Cys binding site spanning the three helices at residues 18, 28, and 67 (the same positions previously used for α_3DIV and α_3DH3) with a nearby Met residue at position 72. α_3DCH3 and α_3DCH4 were designed with chelate motifs

of CXXH or HXXC respectively on helix 1 with His and Met ligands divided among the two remaining helices. Lastly, the α_3DChC2 design repositions the metal binding site of α_3DCH4 further towards the N-terminus of the peptide and the center of the hydrophobic core and encloses it within a “box” of hydrophobic residues in an attempt to enforce an entatic or rack state similar to native T1 Cu proteins.

CD analysis and GuHCl denaturation found that all four constructs were expectedly alpha helical and well folded in solution with the exception of α_3DChC2. Cu(II) UV-Vis and EPR spectroscopies were explored to determine how well each construct had recapitulated the Cu(II) geometry of a T1 Cu protein. α_3DCR1 exhibited spectra similar to those of a type 2 copper-thiolate species with a pronounced LMCT band at 380 nm and a shoulder at 550 nm with a $\varepsilon_{\sigma/\pi}$ ratio of 3.6 and hyperfine coupling constant of 163×10^{-4} cm^{-1}. α_3DCH3 formed a yellow species with an intense band at 400nm, a broad band between 600–800nm resulting in an extremely high $\varepsilon_{\sigma/\pi}$ of 11.9 and hyperfine coupling constant of 152×10^{-4} cm^{-1}. α_3DCH4 had absorption bands at 377, 450 and 520 nm with a $\varepsilon_{\sigma/\pi}$ ratio of 3.3 with an $A_{\|}$ of 185×10^{-4} cm^{-1}. Interestingly a simple flip of a chelate motif from CH3 to CH4 had drastically changed the Cu(II) spectroscopy. We hypothesized that this change was caused by the more buried position of the metal binding site Cys when this chelate motif is flipped. This lead to the design of α_3DChC2 which buried this Cys even further and attempted to create a hydrophobic box around the bound Cu. α_3DChC2 has two intense bands at 401 and 499 nm producing a red-brown copper species with a $\varepsilon_{\sigma/\pi}$ of 2.2 and a slightly compressed hyperfine coupling constant of 130×10^{-4} cm^{-1}. The optical spectroscopy of this construct is reminiscent of variant blue copper protein constructs such as M121E azurin or M148E rusticyanin as well as the native red copper protein nitrosocyanin.[82–83]

One of the most striking results from this study was that all four constructs recapitulated the Cu(I) geometry of a blue copper protein regardless of how successful that construct was at recapitulating the Cu(II) geometry and spectroscopy. Cu(I) EXAFS of all four constructs exhibited short Cu-Cys distances between 2.18–2.22 Angstroms with long distance scatterers observed from His ligation. Analysis of the Cu(I) XANES 1s → 4p transition at 8984eV of all four constructs put the constructs into two groups: ChC2 and CR1 being more 3-coordinate while CH3 and CH4 were more 4-coordinate. Using protein film voltammetry we determined that all four constructs were also successful in modeling the redox potential of a blue copper protein with potentials ranging between 364–462 mV well within the range of native blue copper proteins (300 to 730 mV).[81b, 83b, 84]

These studies showed that the design of the cupredoxin site within a 3HB could have drastic effects on the bound Cu(II) spectroscopy. Our designs culminated in α_3DChC2 which successfully recapitulated the spectroscopy of a red copper protein with the Cu(I) geometry and redox potential of a blue copper protein. We postulated that a more complete understanding of the metal binding site created by α_3DChC2 would allow us to tune this construct’s Cu(II) spectroscopy to those of a green or blue copper protein. That the Cu(I) geometry and redox potential of these constructs remained invariant across our designs indicates that if one were able to tune the Cu(II) spectroscopy of the construct towards that blue copper protein goal the other parameters would already be in place.

Our success with recapitulating a red copper protein with α_3DChC2 lead us to revisit this construct and explore the origins of this spectroscopy to gain clues to how it might be tuned to green or blue copper protein spectroscopies. One possibility was that the relative instability of α_3DChC2 as determined by chemical denaturation may have weakened the hydrophobic box meant to create an entatic state. This instability also precluded any single site mutation studies to investigate this construct so a more stable variant was necessary. Our experience with three stranded coiled coils lead to the strategy of increasing the scaffold protein α_3D's alpha helical length to improve its thermodynamic stability.[85] The initial design of the α_3D scaffold by the De Grado lab went through several iterations of redesign largely centered around the loop region connecting each helix. For our design of GRα_3D we sought to avoid this complication by expanding the helices from the center and duplicating the central heptad of each. GuHCl denaturation of GRα_3D proved this strategy was successful, creating a scaffold with a free energy of unfolding of 11.4 kcal/mol compared to the 5.9 kcal/mol of the parent α_3D. This increased stability allowed us to grow diffraction quality crystals and solve the scaffold's structure to 1.34 Å resolution, a further boon to our design efforts.

Designing the ChC2 binding center into GRα_3D we created GRα_3DChC2 and determined it to be fully folded in solution unlike its parent peptide. The Cu(II) spectroscopy of this construct, however, remained decidedly within the category of a red copper protein, negating the hypothesis that thermodynamic instability had been the cause of α_3DChC2's absorption spectrum. MCD deconvolution of the optical spectrum of GRα_3DChC2 further cemented this red copper protein assignment, matching the d-d electronic transitions observed in native nitrosocyanin.[76] Nitrosocyanin's His_2CysGlu binding site was not a part of our original α_3DChC2 design so the question remained, why was this construct so similar to nitrosocyanin when its design was solely a His_2Cys binding site?

Modelling the binding site of GRα_3DChC2 using the structure of its scaffold we found that because the binding site was designed to span only two helices this positioned the Cu off-center from the hydrophobic interior and more towards the alpha helical interface. Cu positioning at this interface would bring it within ~5 Å from Glu41, included in the GRα_3D scaffold as part of a salt bridge with Arg24. This was a particularly intriguing possibility as GRα_3DChC2's absorption spectrum resembled that of not only nitrosocyanin but the variant blue copper proteins M121E azurin or M148E rusticyanin so it was possible that removing this Cu-Glu41 interaction through a E41A mutation or tuning it with E41Q could allow us to tune the spectroscopy of GRα_3DChC2 to that of a blue or green copper protein.[82–83]

Mutation studies around this Glu41 Arg24 pair found that E41A and E41Q caused drastic changes to the absorption profile; blue shifting the σ LMCT and increasing the $\varepsilon_{\sigma/\pi}$ to 5.3 or 5.7 respectively while the hyperfine coupling constant increased to 160 or 154 × 10^{-4} cm^{-1}. These changes indicated a change from a red copper protein to a type 2 Cu protein. R24A and R24M constructs were made to test if the effects of E41 mutations were caused by the loss of a salt bridge interaction and increased solvent access rather than the loss of a direct interaction between Cu and E41. R24 variant constructs showed no change to their Cu(II) UV-Vis or EPR spectroscopy confirming that the E41A and E41Q mutations had disrupted some kind of E41-Cu interaction. This result confirmed that our GRα_3DChC2 construct was

best thought of as a nitrosocyanin mimic rather than a variant blue copper protein with a Glu in the axial position. This means that tuning this construct to have the spectroscopy of a blue copper protein will likely require larger changes of the active site, possibly as a reverse of a recent construct made by the Lu lab in which the blue copper protein Azurin was mutated to a nitrosocyanin-like red copper construct through rotation of the active site and substitution of the fourth Cu ligand.[86] Furthering our investigation of Cu(I) geometry and redox potential from the previous study both were found to be invariant to all of the mutations tested within this study. This reaffirms the prior assumption that one need only tune the Cu(II) spectroscopy without considering how that may impact Cu(I) geometry or redox potential. We have since used this new structural insight to create variants with green copper protein spectroscopy that can be tuned to blue using chloride as an exogenous ligand similar to the work of Shiga and Tanaka as well as a variant that recapitulates blue copper protein spectroscopy without the need of an exogenous ligand.[77d] A manuscript for this work is in preparation.[87]

4.3 Measuring electron transfer activity

One of the overarching goals of our lab has been to create a fully functional and self-contained Cu Nitrite reductase including a T2 Cu active site and an electron transfer site. This goal requires an understanding of how electron transfer occurs through our peptides as well as the electron transfer rates of our redox active metal centers. To date we have explored this in two ways, using intermolecular ET to study α_3DCH3 and intramolecular ET to look at how electrons can travel through our constructs.[88]

To investigate the electron transfer properties of one of our cupredoxin models, solutions of α_3DCH3 were photooxidized by irradiating Ruthenium(II) trisbipyridine, $[Ru(II)(bipy)_3]^{3+}$, with 460nm laser light in the presence of the electron acceptor $[Ru(III)(NH_3)_6]^{3+}$ to produce $[Ru(III)(bipy)_3]^{3+}$, a powerful oxidizing agent with a reduction potential of 1.3 V. Electron transfer between differing species was then followed by optical spectroscopy. During this reaction the $[Ru(II)(bipy)_3]^{3+}$ radical is formed after 100 nanoseconds which reacts with the electron acceptor to form $[Ru(III)(bipy)_3]^{3+}$ at 1 microsecond. A positive absorption band at 400 nm and 100 microseconds was assigned as the formation of Cu(II)α_3DCH3 from the spectroscopically silent Cu(I)α_3DCH3 while this Cu(II)α_3DCH3 reacted with the electron acceptor to reform Cu(I)α_3DCH3 after 10 milliseconds. Based on the absorption changes we estimated that around 1.9 μM Cu(II)α_3DCH3 was formed from 3 μM $[Ru(III)(bipy)_3]^{3+}$. Reactions using other photoactive oxidants followed similar profiles.

Kinetic analysis found that the first order rate constant of the intermolecular ET reaction between $Ru(III)(bipy)_3$ and Cu(I)α_3DCH was $1.15 \times 10^5\ s^{-1}$, four times greater than the same reaction with apo-peptide. This first order rate constant varied between 0.79 and $1.15 \times 10^5\ s^{-1}$ depending on the photooxidant used. We hypothesized that the reaction between apo-α_3DCH and $[Ru(III)(bipy)_3]^{3+}$ was due to the presence of redox active residues Cys21, His18/28 and Met72 near the C-terminus of the peptide and, due to its relatively low potential, Cys21 was the most likely candidate. This is consistent with native cupredoxins in which the Cu-Cys bond acts as an electron conduit.

Bimolecular rate constants for the electron transfer from Cu(I)α_3DCH to various photooxidants was 8 to 11 × 10^8 M^{-1} s^{-1} indicating diffusion-controlled kinetics and comparable with native cupredoxins under similar conditions exemplifying the success of this *de novo* cupredoxin model. Finally, a comparison of rate to the driving force of five different photooxidants enabled us to calculate the reorganization energy of Cuα_3DCH3 as 1.1 eV. This is on the higher end of the range seen for native cupredoxins (0.7 – 1.2 eV).[89]

Comparing to small molecule complexes like $[Cu(phen)_2]^{2+}$ which changes geometry from tetrahedral to pure tetragonal with a reorganization energy of 2.4 eV we hypothesized that Cuα_3DCH was likely transitioning from a pseudo tetrahedral to pseudotetragonal. These results further emphasize that future designs should focus on forcing the Cu(II) geometry of the construct into an entatic state like native blue copper proteins as previous studies indicate that our constructs are already in the Cu(I) geometry of those proteins.

A self-contained de novo CuNiR model with T1 and T2 Cu centers for electron transfer and enzymatic activity respectively would require an understanding of how electrons will travel through our constructs from one metal center to another. Electron transfer over long distances (~30 Å) is a requirement in various biological systems such as photosynthesis and respiration.[90] Such long distance transfers occur through a series of hops which reduce the distance required for any single electron transfer and increases the rate of the overall process.[91] Proteins can facilitate such hops through redox-active amino acids like Tyr and Trp.[92] Tyrosine radical formation in particular is a vital part of photosystem II, ribonucleotide reductase, and Cytochrome C Oxidase.[90] ET through tyrosine radical formation occurs in a proton coupled fashion because of the large differences in pKa between Tyr (10) and it's radical (−2).[93] The study of natural systems which utilize Tyr radicals is complicated by the complexity of those systems. Previous studies of Tyr radical formation within a designed protein found that a single Tyr radical within an alpha helical bundle can be stabilized through burial in the hydrophobic interior of the peptide.[94] We covalently attached a Ru(II)$(bipy)_3$ photo-oxidant on the C-terminal end of our α_3DH_3 carbonic anhydrase construct to investigate how Tyr hopping could be utilized within our systems to facilitate long distance electron transfer.[88b] Based on the solution structure of α_3D we estimated that the bound Ru and Tyr70 (the closest Tyr) were ~16Å apart.

Laser flash photolysis was used to investigate the ns timescale electron transfer reaction and kinetics between the bound Ru and Ty70. The intermolecular ET between the radical Ru(II)$(bipy)_3$ and the electron acceptor Ru(III)$(NH_3)_6$ produced the oxidized Ru(II)$(bipy)_3$ with second order rate constant of 1.1 × 10^9 M^{-1} s^{-1} (half-life of 40ns). A second phase with a rate of 3.3 × 10^5 s^{-1} was determined to be Tyr radical formation based on the observed absorption maxima at 390 and 410nm.[94a, 95] The observed rate is consistent with that expected for a ET of 16 Å based on a simplified model of electron tunneling in peptides.[96] Finally, a third phase occurs with a half-life of 210 μs in which the Tyr radical combined with the electron acceptor Ru(III)$(NH_3)_6$. pH dependence of the 2nd phase determined it was a PCET as it was four times faster at pH 9.5 than at 5.0 and the presence of a Tyr radical was confirmed through X-band EPR of a reaction in the presence of the nonreversible electron acceptor $[Co(III)(NH_3)_5Cl]^{2+}$. Future directions of this model will design hydrogen bonding amino acids around Tyr70 to investigate their effect on the observed PCET rate and the

distance dependence of designed ET relays. Refining the design of ET relays within alpha helical bundle scaffolds will bring us that much closer to our overall goal of a self-contained de novo NiR model.

5. Summary and Outlook

This review summarizes our recent efforts to generate metalloprotein active sites in *de novo* peptides and proteins composed of three α helices. We have developed several models of metal binding sites with modest to excellent activity towards the native chemistry. Specifically, we have, thus far, targeted the hydrolytic activity of zinc bound to symmetric $(His)_3$ environments, copper nitrite reductase activity, and electron transfer sites within our three α helix scaffolds.

Our approach to generate hydrolytic activity in *de novo* scaffolds that models the activity of CA, whereby we insert a tris(histidine) metal binding environment within our well-defined scaffolds, has revealed interesting features of this enzyme. First, much of the activity arises from the symmetric primary coordination sphere being within a peptidic environment. We were able to exceed small molecule models of CA activity by using the native coordinating ligands, in a more native like system, while still exploring the dependence of activity on overall protein fold. Native CA is composed primarily of beta-sheet and loop structure, yet in the completely alien alpha-helical scaffolds described here, modest to excellent CO_2 hydration and pNPA hydrolysis rates can be obtained. Our next generation hydrolytic active sites will introduce asymmetry in the second coordination sphere, by formation of heterotrimers in our 3SCC system[63] or rational positioning of hydrogen bonding residues in our α_3DH_3 system. Additionally, we can control the orientation of the amino acids residues in proximity to the metal binding site through inclusion of non-natural amino acids or non-canonical repeats, such as stutter and stammer inserts, in the heptads.

As with the $Zn(His)_3$ hydrolytic activities, the successful recapitulation of CuNiR activity has, thus far, only included explicit modelling of the primary coordinating ligands, the (His_3) environment. As with CA, CuNiR possess a critical acid-base H-bonding residue, Asp98, which is required for efficient proton transfer. We had attempted to include Asp in the 3SCC core near the copper site, through our L19D and L26D modifications, though evidence suggested that the carboxylates interacted with each other rather than with the copper site. A consequence of working in our self-associating 3SCC is that our modifications are symmetric. It may be possible to generate better CuNiR activities by positioning only a single Asp above or below the copper site. We have recently described a system where we should be able to make these asymmetric modifications in our 3SCC system, by forming heterotrimeric 3SCCs.[63] Inclusion of non-natural amino acids beyond simple methylated histidine should allow us to tune reduction potentials and Lewis acidity of our metal binding sites.

Finally, we find it interesting to note that rubredoxin and cupredoxin both have binding sites that are comprised of loops. This allows for the binding geometry to be largely dictated by the metal rather than the protein matrix. Creating the same metal coordination within the more rigid scaffold of a helical bundle likely requires exact design, which is a limiting factor

in our strategy whereby we replace leucine residues in the layers of the hydrophobic interior, severely limiting the number of geometric arrangements of ligating residues. Thus, further enhancement to the activities of our electron transfer sites will likely require specific design of the loop regions that connect the helices in α_3D or GRα_3D, or will require a new scaffold that possess additional inherent flexibility or secondary structure elements.

Protein design is a powerful tool to both challenge our understanding of metalloprotein systems and expand our knowledge of metalloenzymatic activity. The ability to recapitulate native metalloprotein function in a vastly different protein architecture, both for catalytic and electron transfer metal sites, highlights a possible pathway for the evolutionary development of the various metalloproteins that are essential for so many cellular functions.

Acknowledgements

T.B.J.P thanks the National Science Research Council of Canada for support in the form of a Postdoctoral Fellowship. V.L.P. thanks the National Institutes of Health for financial support of this research (ES012236). Use of the Stanford Synchrotron Radiation Lightsource, SLAC National Accelerator Laboratory, is supported by the U.S. Department of Energy, Office of Science, Office of Basic Energy Sciences under Contract No. DE-AC02–76SF00515. The SSRL Structural Molecular Biology Program is supported by the DOE Office of Biological and Environmental Research, and by the National Institutes of Health, National Institute of General Medical Sciences (including P41GM103393). The contents of this publication are solely the responsibility of the authors and do not necessarily represent the official views of NIGMS or NIH.

Biographies

Tyler B.J. Pinter received his PhD. from the University of Western Ontario (London, Ontario, Canada) working with Professor Martin Stillman on the metal binding properties of metallothionein examined with electrospray ionization mass spectrometry. He is currently an NSERC funded research fellow working with Professor Vincent Pecoraro on developing *de novo* designed models of metal binding sites.

Karl J. Koebke obtained his PhD from the University of Wisconsin – Milwaukee working with Prof. Andy Pacheco exploring the kinetics of nitric oxide dioxygenation in heme proteins. He then spent three years working as a postdoc in the lab of Vincent Pecoraro where he designed a plethora of *de novo* constructs including nitrite reductase and cupredoxin mimics. After a year working with Prof. Timothy Stemmler on mitochondrial FeS cluster biogenesis he is now working with Prof. Neil Marsh on self-assembling protein nano-cages.

Vincent L. Pecoraro is the John T. Groves Collegiate Professor of Chemistry at the University of Michigan, Ann Arbor. He is an expert in bioinorganic and supramolecular chemistries, having made substantive contributions to the understanding of photosynthetic water oxidation and vanadium biochemistry. In recent years he has been a leader in the field of metalloprotein design and the development of metallacrowns as biomolecular imaging agents. He served as an Associate Editor for *Inorganic Chemistry* for over 20 years and is a fellow of both the ACS and AAAS.

References

[1]. a)Waldron KJ, Rutherford JC, Ford D, Robinson NJ, Nature 2009, 460, 823; [PubMed: 19675642] b)Bertini I, Sigel A, Handbook on Metalloproteins, CRC Press, 2001;c)Andreini C, Bertini I, Cavallaro G, Holliday GL, Thornton JM, J. Biol. Inorg. Chem 2008, 13, 1205–1218. [PubMed: 18604568]

[2]. Andreini C, Bertini I, Rosato A, Acc. Chem. Res 2009, 42, 1471–1479. [PubMed: 19697929]

[3]. a)Huang P-S, Boyken SE, Baker D, Nature 2016, 537, 320; [PubMed: 27629638] b)Yu F, Cangelosi VM, Zastrow ML, Tegoni M, Plegaria JS, Tebo AG, Mocny CS, Ruckthong L, Qayyum H, Pecoraro VL, Chem. Rev 2014, 114, 3495–3578; [PubMed: 24661096] c)Lu Y, Berry SM, Pfister TD, Chem. Rev 2001, 101, 3047–3080; [PubMed: 11710062] d)Lu Y, Yeung N, Sieracki N, Marshall NM, Nature 2009, 460, 855; [PubMed: 19675646] e)Nastri F, D'Alonzo D, Leone L, Zambrano G, Pavone V, Lombardi A, Trends Biochem. Sci

[4]. Smith BA, Hecht MH, Curr. Opin. Chem. Biol 2011, 15, 421–426. [PubMed: 21474363]

[5]. Kaplan J, DeGrado W, Proc. Natl. Acad. Sci. U.S.A 2004, 101, 11566–11570. [PubMed: 15292507]

[6]. Woolfson DN, Bartlett GJ, Burton AJ, Heal JW, Niitsu A, Thomson AR, Wood CW, Curr. Opin. Struct. Biol 2015, 33, 16–26. [PubMed: 26093060]

[7]. a)Schneider JP, Lombardi A, DeGrado WF, Fold. Des 1998, 3, R29–R40; [PubMed: 9565750] b)Moutevelis E, Woolfson DN, J. Mol. Biol 2009, 385, 726–732. [PubMed: 19059267]

[8]. Lovejoy B, Choe S, Cascio D, McRorie D, DeGrado W, Eisenberg D, Science 1993, 259, 1288–1293. [PubMed: 8446897]

[9]. Hodges RS, Saund AK, Chong PC, St-Pierre SA, Reid RE, J. Biol. Chem 1981, 256, 1214–1224. [PubMed: 7451500]

[10]. Dieckmann GR, McRorie DK, Tierney DL, Utschig LM, Singer CP, O'Halloran TV, Penner-Hahn JE, DeGrado WF, Pecoraro VL, J. Am. Chem. Soc 1997, 119, 6195–6196.

[11]. Koebke KJ, Ruckthong L, Meagher JL, Mathieu E, Harland J, Deb A, Lehnert N, Policar C, Tard C, Penner-Hahn JE, Inorg. Chem 2018, 57, 12291–12302. [PubMed: 30226758]

[12]. Zastrow ML, Peacock AF, Stuckey JA, Pecoraro VL, Nat. Chem 2012, 4, 118.

[13]. Plegaria JS, Dzul SP, Zuiderweg ER, Stemmler TL, Pecoraro VL, Biochemistry 2015, 54, 2858–2873. [PubMed: 25790102]

[14]. Holm RH, Kennepohl P, Solomon EI, Chem. Rev 1996, 96, 2239–2314. [PubMed: 11848828]

[15]. a)Liu J, Chakraborty S, Hosseinzadeh P, Yu Y, Tian S, Petrik I, Bhagi A, Lu Y, Chem. Rev 2014, 114, 4366–4469; [PubMed: 24758379] b)Shaik S, Munro AW, Sen S, Mowat C, Nam W, Derat E, Bugg T, Proshlyakov DA, Hausinger RP, Straganz GD, Iron-containing enzymes: Versatile catalysts of hydroxylation reactions in nature, Royal Society of Chemistry, 2011;c)Lill R, Nature 2009, 460, 831; [PubMed: 19675643] d)Andreini C, Putignano V, Rosato A, Banci L, Metallomics 2018, 10, 1223–1231. [PubMed: 30095136]

[16]. a)Lee K-H, Matzapetakis M, Mitra S, Marsh ENG, Pecoraro VL, J. Am. Chem. Soc 2004, 126, 9178–9179; [PubMed: 15281796] b)Ruckthong L, Deb A, Hemmingsen L, Penner-Hahn JE, Pecoraro VL, J. Biol. Ionrg. Chem 2018, 23, 123–135;c)Peacock AF, Hemmingsen L, Pecoraro VL, Proc. Natl. Acad. Sci. U.S.A 2008, 105, 16566–16571; [PubMed: 18940928] d)Peacock AF, Stuckey JA, Pecoraro VL, Angew. Chem. Int. Ed 2009, 48, 7371–7374.

[17]. Håkansson K, Carlsson M, Svensson LA, Liljas A, J. Mol. Biol 1992, 227, 1192–1204. [PubMed: 1433293]

[18]. a)Kimura E, Shiota T, Koike T, Shiro M, Kodama M, J. Am. Chem. Soc 1990, 112, 5805–5811;b)Olmo CP, Böhmerle K, Vahrenkamp H, Inorg. Chim. Acta 2007, 360, 1510–1516;c)Koerner TB, Brown R, Can. J. Chem 2002, 80, 183–191.

[19]. a)Kiefer LL, Paterno SA, Fierke CA, J. Am. Chem. Soc 1995, 117, 6831–6837;b)Krebs JF, Ippolito J, Christianson D, Fierke C, J. Biol. Chem 1993, 268, 27458–27466; [PubMed: 8262987] c)Liang Z, Xue Y, Behravan G, Jonsson BH, Lindskog S, Eur. J. Biochem 1993, 211, 821–827. [PubMed: 8436138]

[20]. Der BS, Edwards DR, Kuhlman B, Biochemistry 2012, 51, 3933–3940. [PubMed: 22510088]

[21]. Zastrow ML, Pecoraro VL, J. Am. Chem. Soc 2013, 135, 5895–5903. [PubMed: 23516959]

[22]. Eriksson AE, Jones TA, Liljas A, Proteins: Struct., Funct., Bioinf 1988, 4, 274–282.

[23]. Matzapetakis M, Farrer BT, Weng T-C, Hemmingsen L, Penner-Hahn JE, Pecoraro VL, J. Am. Chem. Soc 2002, 124, 8042–8054. [PubMed: 12095348]

[24]. Cangelosi VM, Deb A, Penner-Hahn JE, Pecoraro VL, Angew. Chem. Int. Ed 2014, 53, 7900–7903.

[25]. Jackman JE, Merz KM, Fierke CA, Biochemistry 1996, 35, 16421–16428. [PubMed: 8987973]

[26]. Jewell DA, Tu C, Paranawithana SR, Tanhauser SM, LoGrasso PV, Laipis PJ, Silverman DN, Biochemistry 1991, 30, 1484–1490. [PubMed: 1899618]

[27]. Koziol L, Valdez CA, Baker SE, Lau EY, Floyd III WC, Wong SE, Satcher JH Jr, Lightstone FC, Aines RD, Inorg. Chem 2012, 51, 6803–6812. [PubMed: 22671132]

[28]. Nakata K, Shimomura N, Shiina N, Izumi M, Ichikawa K, Shiro M, J. Inorg. Biochem 2002, 89, 255–266. [PubMed: 12062130]

[29]. Slebocka-Tilk H, Cocho J, Frackman Z, Brown R, J. Am. Chem. Soc 1984, 106, 2421–2431.

[30]. Fierke CA, Calderone TL, Krebs JF, Biochemistry 1991, 30, 11054–11063. [PubMed: 1657158]

[31]. Studer S, Hansen DA, Pianowski ZL, Mittl PR, Debon A, Guffy SL, Der BS, Kuhlman B, Hilvert D, Science 2018, 362, 1285–1288. [PubMed: 30545884]

[32]. a)Song WJ, Tezcan FA, Science 2014, 346, 1525–1528; [PubMed: 25525249] b)Brodin JD, Medina-Morales A, Ni T, Salgado EN, Ambroggio XI, Tezcan FA, J. Am. Chem. Soc 2010, 132, 8610–8617. [PubMed: 20515031]

[33]. Rufo CM, Moroz YS, Moroz OV, Stöhr J, Smith TA, Hu X, DeGrado WF, Korendovych IV, Nat. Chem 2014, 6, 303. [PubMed: 24651196]

[34]. Ruckthong L, Zastrow ML, Stuckey JA, Pecoraro VL, J. Am. Chem. Soc 2016, 138, 11979–11988. [PubMed: 27532255]

[35]. a)Iwasaki H, Noji S, Shidara S, J. Biochem 1975, 78, 355–361; [PubMed: 179983] b)Libby E, Averill BA, Biochem. Biophys. Res. Commun 1992, 187, 1529–1535; [PubMed: 1329738] c)Kukimoto M, Nishiyama M, Murphy ME, Turley S, Adman ET, Horinouchi S, Beppu T, Biochemistry 1994, 33, 5246–5252; [PubMed: 8172899] d)Murphy ME, Turley S, Adman ET, J. Biol. Chem 1997, 272, 28455–28460. [PubMed: 9353305]

[36]. a)Antonyuk SV, Strange RW, Sawers G, Eady RR, Hasnain SS, Proc. Natl. Acad. Sci. U.S.A 2005, 102, 12041–12046; [PubMed: 16093314] b)Kataoka K, Furusawa H, Takagi K, Yamaguchi K, Suzuki S, J. Biochem 2000, 127, 345–350; [PubMed: 10731703] c)Boulanger MJ, Kukimoto M, Nishiyama M, Horinouchi S, Murphy ME, J. Biol. Chem 2000, 275, 23957–23964. [PubMed: 10811642]

[37]. Tegoni M, Yu F, Bersellini M, Penner-Hahn JE, Pecoraro VL, Proc. Natl. Acad. Sci. U.S.A 2012, 109, 21234–21239. [PubMed: 23236170]

[38]. Kau LS, Spira-Solomon DJ, Penner-Hahn JE, Hodgson KO, Solomon EI, J. Am. Chem. Soc 1987, 109, 6433–6442.

[39]. Prenesti E, Daniele PG, Prencipe M, Ostacoli G, Polyhedron 1999, 18, 3233–3241.

[40]. Olesen K, Veselov A, Zhao Y, Wang Y, Danner B, Scholes CP, Shapleigh JP, Biochemistry 1998, 37, 6086–6094. [PubMed: 9558347]

[41]. a)Jacobson F, Pistorius A, Farkas D, De Grip W, Hansson Ö, Sjölin L, Neutze R, J. Biol. Chem 2007, 282, 6347–6355; [PubMed: 17148448] b)Suzuki S, Yamaguchi K, Kataoka K, Kobayashi K, Tagawa S, Kohzuma T, Shidara S, Iwasaki H, J. Biol. Ionrg. Chem 1997, 2, 265–274.

[42]. Monzani E, Koolhaas GAA, Spandre A, Leggieri E, Casella L, Gullotti M, Nardin G, Randaccio L, Fontani M, Zanello P, J. Biol. Ionrg. Chem 2000, 5, 251–261.

[43]. Warshel A, Sharma PK, Kato M, Xiang Y, Liu H, Olsson MH, Chem. Rev 2006, 106, 3210–3235. [PubMed: 16895325]

[44]. Fried SD, Bagchi S, Boxer SG, Science 2014, 346, 1510–1514. [PubMed: 25525245]

[45]. a)Zwanzig R, J. Chem. Phys 1992, 97, 3587–3589;b)Min W, English BP, Luo G, Cherayil BJ, Kou S, Xie XS, Acc. Chem. Res 2005, 38, 923–931. [PubMed: 16359164]

[46]. Ross MR, White AM, Yu F, King JT, Pecoraro VL, Kubarych KJ, J. Am. Chem. Soc 2015, 137, 10164–10176. [PubMed: 26247178]

[47]. Lim M, Hamm P, Hochstrasser RM, Proc. Natl. Acad. Sci. U.S.A 1998, 95, 15315–15320. [PubMed: 9860966]

[48]. a)Churg A, Warshel A, Biochemistry 1986, 25, 1675–1681; [PubMed: 3011070] b)Kuila D, Fee JA, J. Biol. Chem 1986, 261, 2768–2771; [PubMed: 3949746] c)Varadarajan R, Zewert TE, Gray HB, Boxer SG, Science 1989, 243, 69–72. [PubMed: 2563171]

[49]. Chufán EE, Prigge ST, Siebert X, Eipper BA, Mains RE, Amzel LM, J. Am. Chem. Soc 2010, 132, 15565–15572. [PubMed: 20958070]

[50]. Yu F, Penner-Hahn JE, Pecoraro VL, J. Am. Chem. Soc 2013, 135, 18096–18107. [PubMed: 24182361]

[51]. Gray HB, Malmström BG, Comments Inorg. Chem 1983, 2, 203–209.

[52]. a)Iranzo O, Cabello C, Pecoraro VL, Angew. Chem. Int. Ed 2007, 46, 6688–6691;b)Lee KH, Cabello C, Hemmingsen L, Marsh ENG, Pecoraro VL, Angew. Chem. Int. Ed 2006, 45, 2864–2868.

[53]. Koebke KJ, Yu F, Salerno E, Van Stappen C, Tebo AG, Penner-Hahn JE, Pecoraro VL, Angew. Chem. Int. Ed 2018, 57, 3954–3957.

[54]. Fukuda Y, Tse KM, Nakane T, Nakatsu T, Suzuki M, Sugahara M, Inoue S, Masuda T, Yumoto F, Matsugaki N, Proc. Natl. Acad. Sci. U.S.A 2016, 113, 2928–2933. [PubMed: 26929369]

[55]. Prigge ST, Kolhekar AS, Eipper BA, Mains RE, Amzel LM, Science 1997, 278, 1300–1305. [PubMed: 9360928]

[56]. Koebke KJ, Yu F, Van Stappen C, Pinter TB, Deb A, Penner-Hahn JE, Pecoraro VL, J. Am. Chem. Soc 2019.

[57]. Tanokura M, Biochim. Biophys. Acta, Protein Struct. Mol. Enzymol 1983, 742, 576–585.

[58]. Tegoni M, Yu F, Bersellini M, Penner-Hahn JE, Pecoraro VL, PNAS 2012, 109, 21234–21239. [PubMed: 23236170]

[59]. Koebke KJ, Yu F, Salerno E, Stappen CV, Tebo AG, Penner-Hahn JE, Pecoraro VL, Angew. Chem. Int. Ed 2018, 57, 3954–3957.

[60]. Isoda N, Yokoyama H, Nojiri M, Suzuki S, Yamaguchi K, Bioelectrochemistry 2010, 77, 82–88. [PubMed: 19616484]

[61]. Tocheva EI, Eltis LD, Murphy MEP, Biochemistry 2008, 47, 4452–4460. [PubMed: 18358002]

[62]. Leferink NGH, Han C, Antonyuk SV, Heyes DJ, Rigby SEJ, Hough MA, Eady RR, Scrutton NS, Hasnain SS, Biochemistry 2011, 50, 4121–4131. [PubMed: 21469743]

[63]. Tolbert AE, Ervin CS, Ruckthong L, Paul TJ, Jayasinghe-Arachchige VM, Neupane KP, Stuckey JA, Prabhakar R, Pecoraro VL, Submitted 2019.

[64]. a)Lovenberg W, Sobel BE, Proc. Natl. Acad. Sci. U.S.A 1965, 54, 193–199; [PubMed: 5216351] b)Bertrand P, Gayda J-P, Biochim. Biophys. Acta 1988, 954, 347–350; [PubMed: 3370220] c)Shulman RG, Eisenberger P, Blumberg WE, Stombaugh NA, Proc. Natl. Acad. Sci. U. S. A 1975, 72, 4003–4007; [PubMed: 1060082] d)Bunker B, Stern EA, Biophys. J 1977, 19, 253–264; [PubMed: 890038] e)Atherton NM, Garbett K, Gillard RD, Mason R, Mayhew SJ, Peel JL,

Stangroom JE, Nature 1966, 212, 590–593; [PubMed: 4291336] f)Bönisch H, Schmidt CL, Bianco P, Ladenstein R, J. Biol. Ionrg. Chem 2007, 12, 1163–1171.

[65]. a)Lee SC, Lo W, Holm RH, Chem. Rev 2014, 114, 3579–3600; [PubMed: 24410527] b)Gerlach DL, Coucouvanis D, Kampf J, Lehnert N, Eur. J. Inorg. Chem 2013, 2013, 5253–5264.

[66]. a)Jacques A, Clémancey M, Blondin G, Fourmond V, Latour J-M, Sénèque O, Chem. Commun 2013, 49, 2915–2917;b)Nanda V, Rosenblatt MM, Osyczka A, Kono H, Getahun Z, Dutton PL, Saven JG, DeGrado WF, J. Am. Chem. Soc 2005, 127, 5804–5805; [PubMed: 15839675] c)Jacques A, Latour J-M, Sénèque O, Dalton Trans 2014, 43, 3922–3930; [PubMed: 24448566] d)Farinas E, Regan L, Protein Sci 1998, 7, 1939–1946; [PubMed: 9761474] e)Benson DE, Wisz MS, Liu W, Hellinga HW, Biochemistry 1998, 37, 7070–7076. [PubMed: 9585516]

[67]. Tebo AG, Pinter TBJ, García-Serres R, Speelman AL, Tard C, Sénéque O, Blondin G, Latour J-M, Penner-Hahn J, Lehnert N, Pecoraro VL, Biochemistry 2018, 57, 2308–2316. [PubMed: 29561598]

[68]. Tebo AG, Hemmingsen L, Pecoraro VL, Metallomics 2015, 7, 1555–1561. [PubMed: 26503746]

[69]. Xiao Z, Lavery MJ, Ayhan M, Scrofani SDB, Wilce MCJ, Guss JM, Tregloan PA, George GN, Wedd AG, J. Am. Chem. Soc 1998, 120, 4135–4150.

[70]. a)Wegner P, Bever M, Schünemann V, Trautwein AX, Schmidt C, Bönisch H, Gnida M, Meyer-Klaucke W, Hyperfine Interact 2004, 156, 293–298;b)Meyer JJM, in Handbook of Metalloproteins (Ed.: Messerschmidt A, R. H; Poulat T; Wieghardt K), 2006.

[71]. a)Moura I, Xavier AV, Cammack R, Bruschi M, Le Gall J, Biochimica et Biophysica Acta (BBA) -Protein Structure 1978, 533, 156–162;b)Jenney FE, Adams MWW, in Methods Enzymol, Vol. 334, Academic Press, 2001, pp. 45–55. [PubMed: 11398483]

[72]. a)Oganesyan VS, George SJ, Cheesman MR, Thomson AJ, J. Chem. Phys 1999, 110, 762–777;b)Yoo SJ, Meyer J, Achim C, Peterson J, Hendrich MP, Münck E, J. Biol. Ionrg. Chem 2000, 5, 475–487;c)Börger B, Suter D, J. Chem. Phys 2001, 115, 9821–9826;d)Peisach J, Blumberg WE, Lode ET, Coon MJ, J. Biol. Chem 1971, 246, 5877–5881. [PubMed: 4330058]

[73]. Solomon EI, Inorg. Chem 2006, 45, 8012–8025. [PubMed: 16999398]

[74]. Gewirth AA, Solomon EI, J. Am. Chem. Soc 1988, 110, 3811–3819.

[75]. LaCroix LB, Shadle SE, Wang Y, Averill BA, Hedman B, Hodgson KO, Solomon EI, J. Am. Chem. Soc 1996, 118, 7755–7768.

[76]. Basumallick L, Sarangi R, DeBeer George S, Elmore B, Hooper AB, Hedman B, Hodgson KO, Solomon EI, J. Am. Chem. Soc 2005, 127, 3531–3544. [PubMed: 15755175]

[77]. a)Hellinga HW, J. Am. Chem. Soc 1998, 120, 10055–10066;b)Lu Y, LaCroix LB, Lowery MD, Solomon EI, Bender CJ, Peisach J, Roe JA, Gralla EB, Valentine JS, J. Am. Chem. Soc 1993, 115, 5907–5918;c)Schnepf R, Haehnel W, Wieghardt K, Hildebrandt P, J. Am. Chem. Soc 2004, 126, 14389–14399; [PubMed: 15521758] d)Shiga D, Nakane D, Inomata T, Funahashi Y, Masuda H, Kikuchi A, Oda M, Noda M, Uchiyama S, Fukui K, Kanaori K, Tajima K, Takano Y, Nakamura H, Tanaka T, J. Am. Chem. Soc 2010, 132, 18191–18198. [PubMed: 21126081]

[78]. Shiga D, Hamano Y, Kamei M, Funahashi Y, Masuda H, Sakaguchi M, Ogura T, Tanaka T, J. Biol. Ionrg. Chem 2012, 17, 1025–1031.

[79]. Plegaria JS, Duca M, Tard C, Friedlander TJ, Deb A, Penner-Hahn JE, Pecoraro VL, Inorg. Chem 2015, 54, 9470–9482. [PubMed: 26381361]

[80]. Chakraborty S, Kravitz JY, Thulstrup PW, Hemmingsen L, DeGrado WF, Pecoraro VL, Angew. Chem. Int. Ed 2011, 50, 2049–2053.

[81]. a)Penfield KW, Gay RR, Himmelwright RS, Eickman NC, Norris VA, Freeman HC, Solomon EI, J. Am. Chem. Soc 1981, 103, 4382–4388;b)Anderson GP, Sanderson DG, Lee CH, Durell S, Anderson LB, Gross EL, Biochim. Biophys. Acta 1987, 894, 386–398. [PubMed: 3689779]

[82]. Arciero DM, Pierce BS, Hendrich MP, Hooper AB, Biochemistry 2002, 41, 1703–1709. [PubMed: 11827513]

[83]. a)Karlsson BG, Tsai L-C, Nar H, Sanders-Loehr J, Bonander N, Langer V, Sjölin L, Biochemistry 1997, 36, 4089–4095; [PubMed: 9100002] b)Hall JF, Kanbi LD, Strange RW, Hasnain SS, Biochemistry 1999, 38, 12675–12680. [PubMed: 10504237]

[84]. a)Pascher T, Karlsson BG, Nordling M, Malmstom BG, Vanngard T, Eur. J. Biochem 1993, 212, 289–296; [PubMed: 8383044] b)Lappin AG, Lewis CA, Ingledew WJ, Inorg. Chem 1985, 24,

1446–1450;c)Xu F, Berka RM, Wahleithner JA, Nelson BA, Shuster JR, Brown SH, Palmer AE, Solomon EI, Biochem. J 1998, 334, 63–70. [PubMed: 9693103]

[85]. a)Farrer BT, Harris NP, Balchus KE, Pecoraro VL, Biochemistry 2001, 40, 14696–14705; [PubMed: 11724584] b)Su JY, Hodges RS, Kay CM, Biochemistry 1994, 33, 15501–15510. [PubMed: 7803412]

[86]. Tian S, Liu J, Cowley RE, Hosseinzadeh P, Marshall NM, Yu Y, Robinson H, Nilges MJ, Blackburn NJ, Solomon EI, Lu Y, Nat. Chem 2016, 8, 670–677. [PubMed: 27325093]

[87]. Koebke KJ, Pinter TBJ, Deb A, Tard C, Penner-Hahn J, Pecoraro VL, In preparation 2019.

[88]. a)Plegaria JS, Herrero C, Quaranta A, Pecoraro VL, Biochim. Biophys. Acta 2016, 1857, 522–530; [PubMed: 26427552] b)Tebo AG, Quaranta A, Herrero C, Pecoraro VL, Aukauloo A, ChemPhotoChem 2017, 1, 89–92. [PubMed: 29046892]

[89]. a)Winkler JR, Wittung-Stafshede P, Leckner J, Malmström BG, Gray HB, Proc. Natl. Acad. Sci. U.S.A 1997, 94, 4246–4249; [PubMed: 9113974] b)Di Bilio AJ, Hill MG, Bonander N, Karlsson BG, Villahermosa RM, Malmström BG, Winkler JR, Gray HB, J. Am. Chem. Soc 1997, 119, 9921–9922;c)Skov LK, Pascher T, Winkler JR, Gray HB, J. Am. Chem. Soc 1998, 120, 1102–1103;d)Sigfridsson K, Ejdebäck M, Sundahl M, Hansson Ö, Arch. Biochem. Biophys 1998, 351, 197–206; [PubMed: 9514646] e)McCleskey TM, Winkler JR, Gray HB, J. Am. Chem. Soc 1992, 114, 6935–6937.

[90]. Dempsey JL, Winkler JR, Gray HB, Chem. Rev 2010, 110, 7024–7039. [PubMed: 21082865]

[91]. a)Gray HB, Winkler JR, Chem. Phys. Lett 2009, 483, 1–9; [PubMed: 20161522] b)Gray HB, Winkler JR, Q. Rev. Biophys 2004, 36, 341–372;c)Moser CC, Keske JM, Warncke K, Farid RS, Dutton PL, Nature 1992, 355, 796–802. [PubMed: 1311417]

[92]. Barry BA, J. Photochem. Photobiol. B 2011, 104, 60–71. [PubMed: 21419640]

[93]. Dixon WT, Murphy D, J. Chem. Soc., Faraday Trans. 2 1976, 72, 1221–1230.

[94]. a)Berry BW, Martínez-Rivera MC, Tommos C, Proc. Natl. Acad. Sci. U.S.A 2012, 109, 9739–9743; [PubMed: 22675121] b)Glover SD, Jorge C, Liang L, Valentine KG, Hammarström L, Tommos C, J. Am. Chem. Soc 2014, 136, 14039–14051. [PubMed: 25121576]

[95]. a)Candeias LP, Turconi S, Nugent JHA, Biochim. Biophys. Acta 1998, 1363, 1–5; [PubMed: 9526027] b)Pizano AA, Lutterman DA, Holder PG, Teets TS, Stubbe J, Nocera DG, Proc. Natl. Acad. Sci. U.S.A 2012, 109, 39–43. [PubMed: 22171005]

[96]. Moser CC, Dutton PL, Biochim. Biophys. Acta 1992, 1101, 171–176. [PubMed: 1633183]

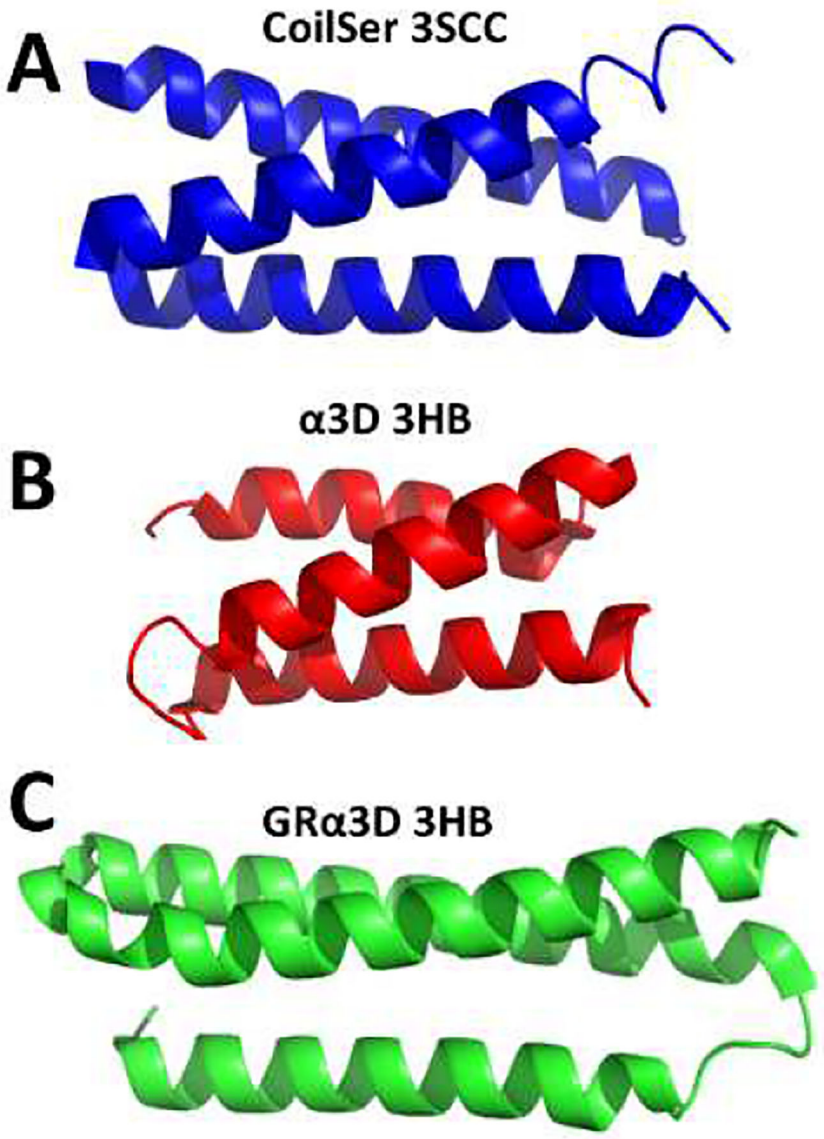

Figure 1:

Structures of the peptide and protein scaffolds that will be discussed in this review: TRI crystallographic analogue CoilSer (A, PDB 3PBJ[12]), α_3D (B, PDB 2MTQ[13]), and GRα_3D (C, PDB 6DS9[11]).

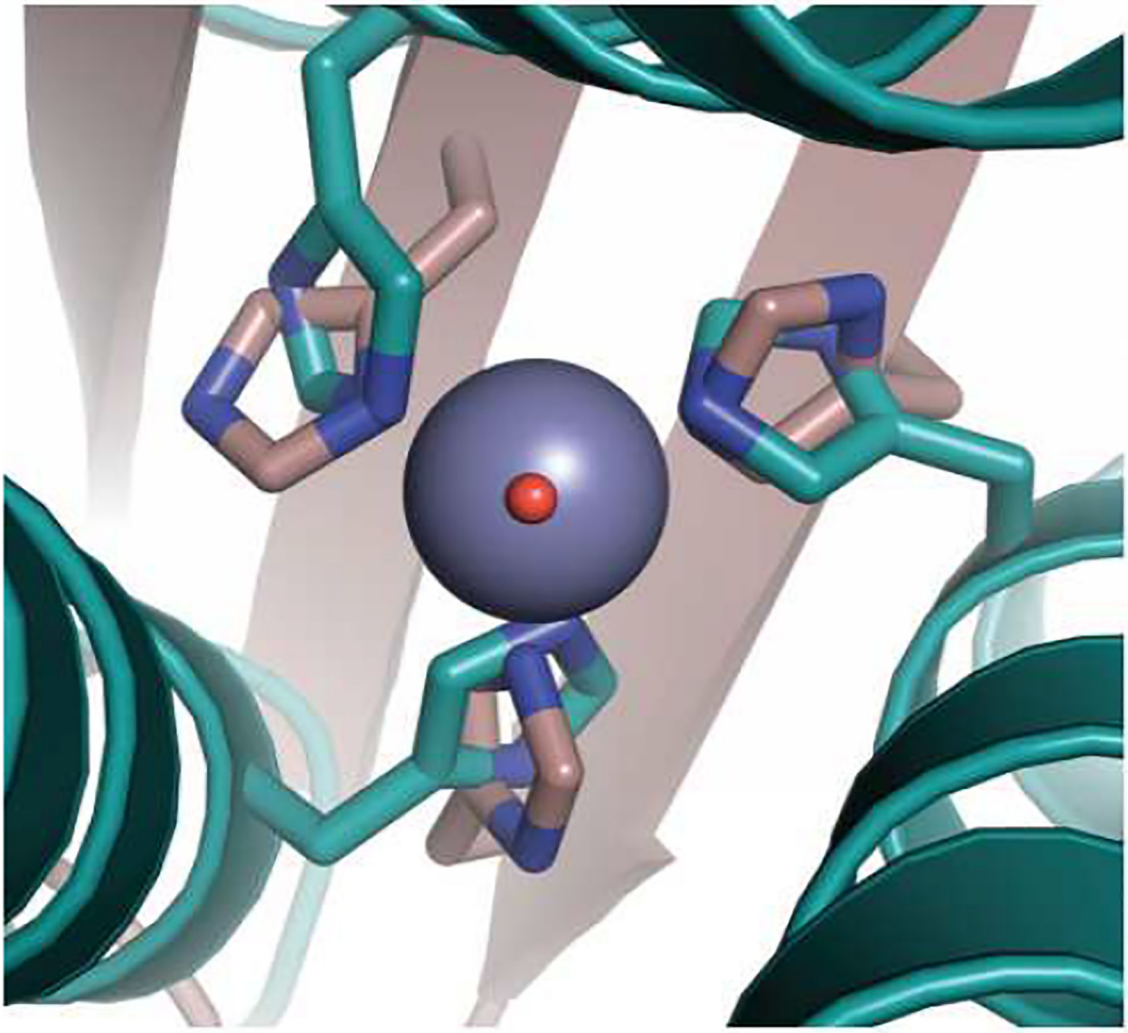

Figure 2:

Overlay of the Zn(II)N_3O site in $[Hg(II)]_S[Zn(II)(H_2O)]_N$ $(CSL9PenL23H)_3$ with the active site of human CAII. CS is shown in cyan (PDB 3PBJ[12]) and CAII in tan (PDB 2CBA[17]). The solvent molecule associated with CS is shown in red and that associated with CAII lies below the zinc. Reprinted with permission from ref [12]. Copyright 2012 Nature Publishing Group.

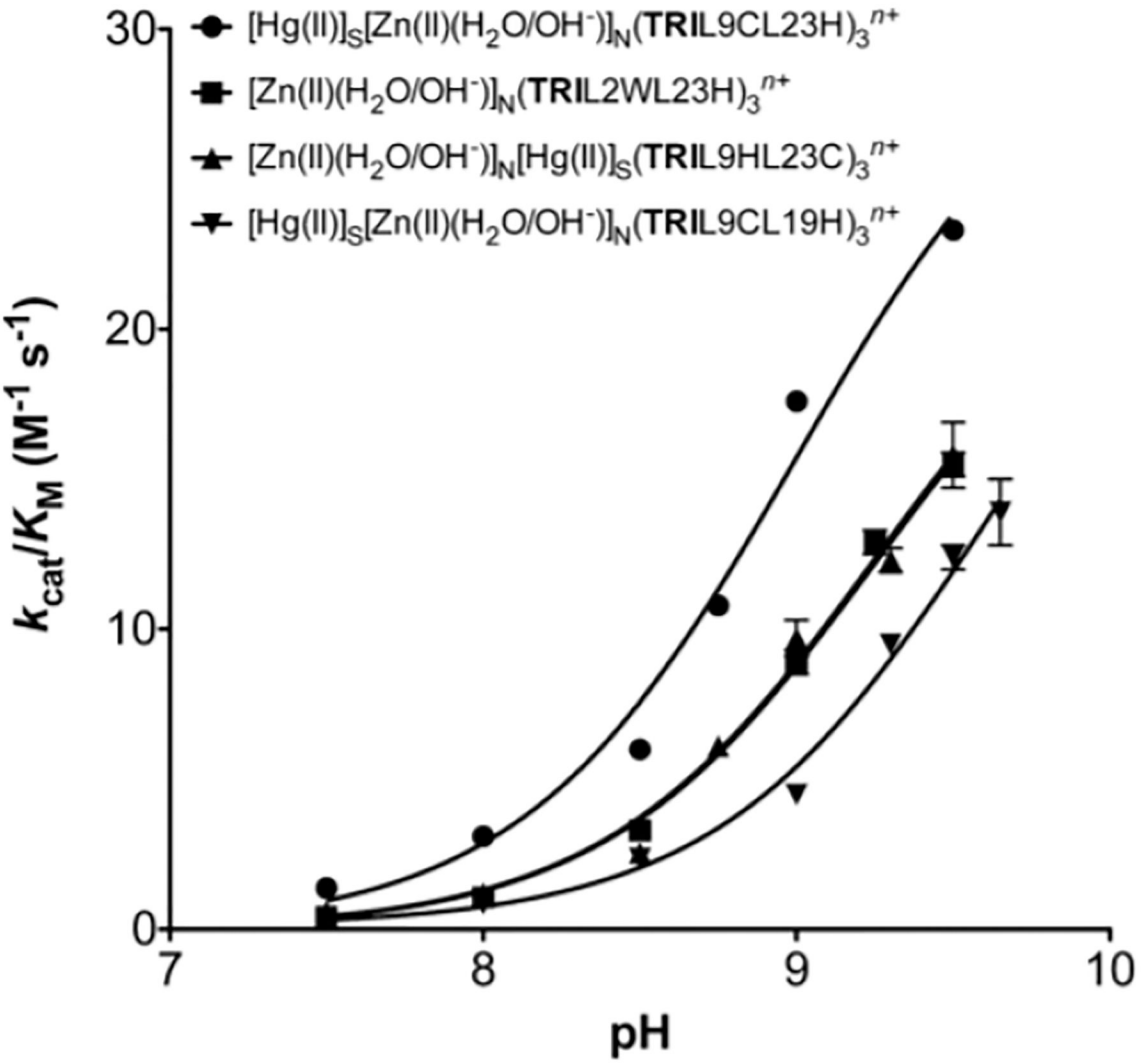

Figure 3:

pH dependency of the catalytic efficiency for pNPA hydrolysis by Zn(II)-bound TRI peptides: $[Hg(II)]_S[Zn(II)]_N$-TRIL9CL23H (●), $[Zn(II)]_N$-TRIL2WL23H (■), $[Zn(II)]_N[Hg(II)]_S$-TRIL9HL23C (▲), and $[Hg(II)]_S[Zn(II))]_N$-TRIL9CL19H (▼). Reprinted with permission from ref [12]. Copyright 2013 American Chemical Society.

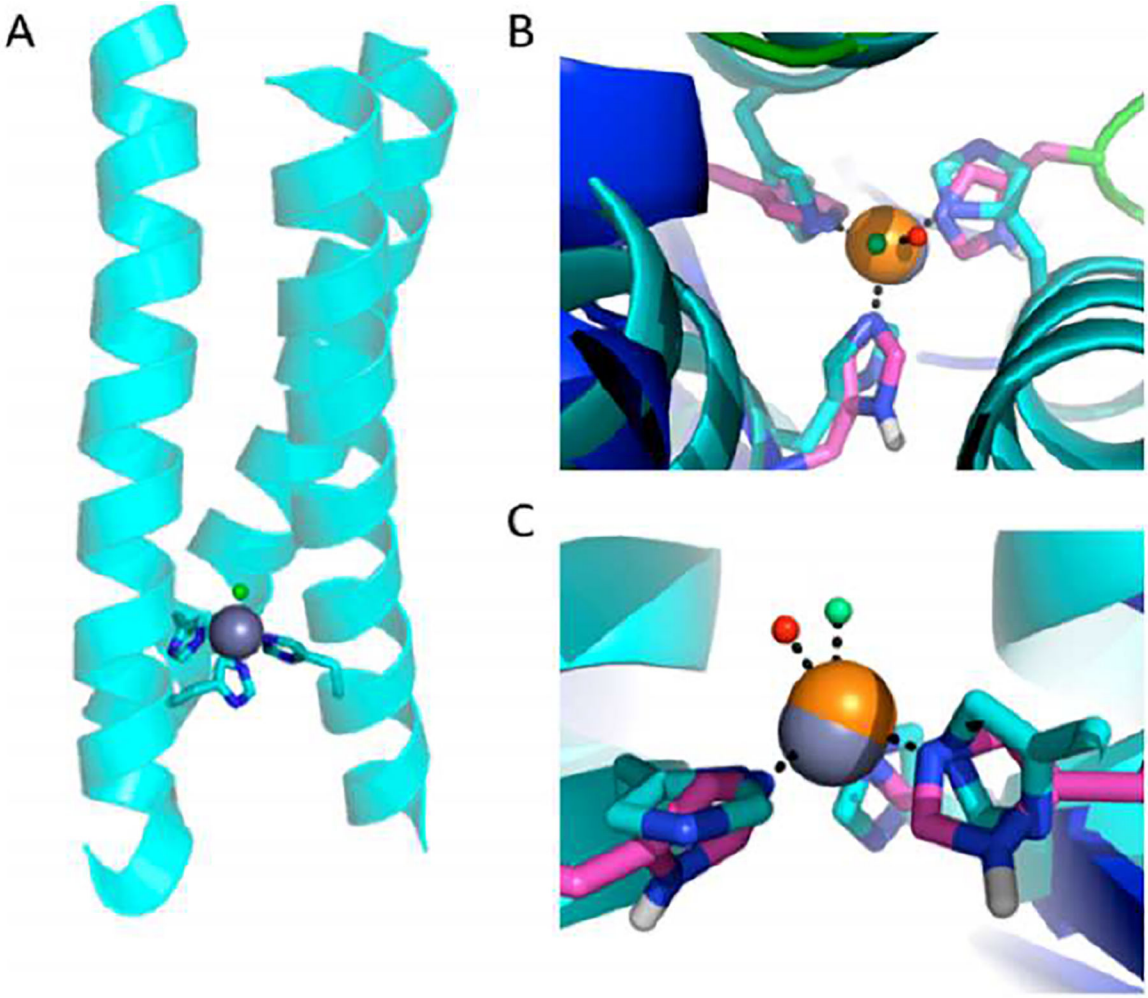

Figure 4:

(A) Model of Cu-TRIL23H based on the structure of $Hg(II)_S Zn(II)_N$CSL9CL23H. (B) View of the $Zn(II)(H_2O)(His)_3$ site along the pseudo three-fold axis (light gray), superimposed to the type 2 $Cu(II)(H_2O)(His)_3$ site in *R. sphaeroides* NiR (PDB ID code 2DY2) (dark gray). Coordinated water molecules are shown as spheres. (C) Side view of the two metal sites, as in B. Reprinted and adapted with permission from ref [37]. Copyright 2012 Proceedings of the National Academy of Sciences of the United States of America.

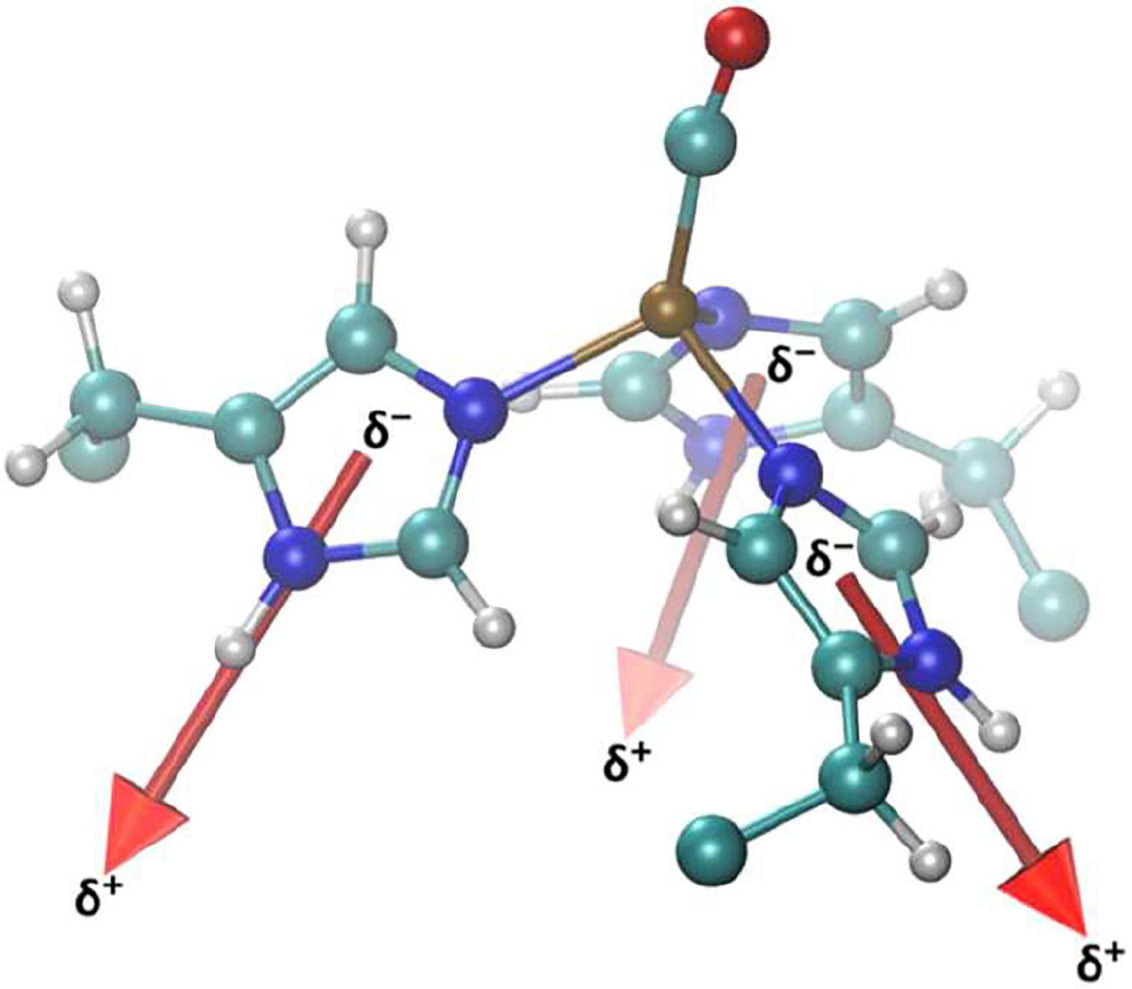

Figure 5:
Dipole moment of each histidine ring, in Cu(I) (TRIL2WL23H)3(CO)+ with average magnitude of 3.6 D. These dipolar side chains are able to couple to the electrostatic environment produced by the protein scaffold. Reprinted with permission from ref [46]. Copyright 2013 American Chemical Society.

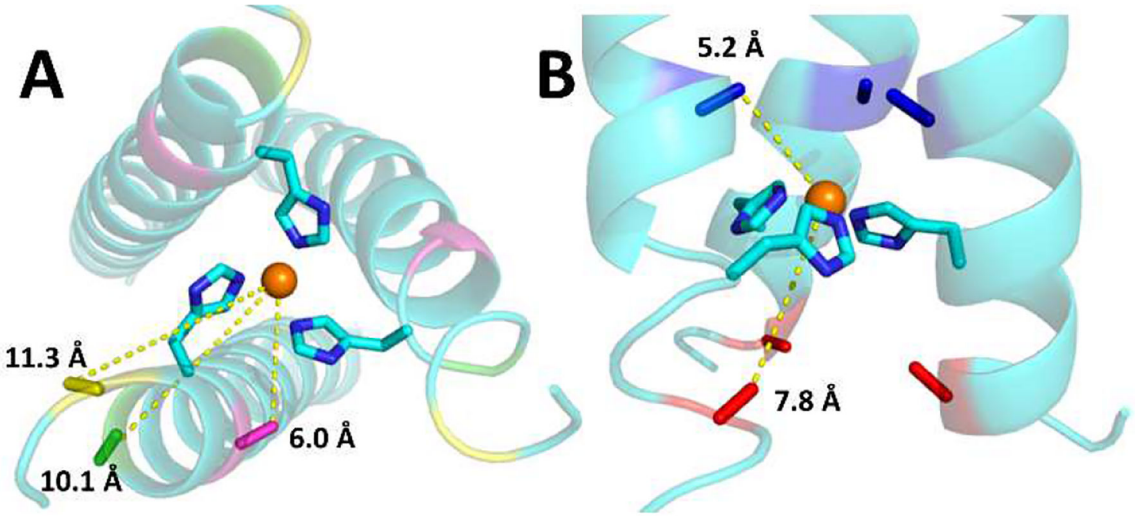

Figure 6:

Model of CuNiR highlighting the location of outer sphere (A) and inner sphere (B) residue substitutions near the Cu binding site of TRI-H based on the crystal structure of $Zn^{II}_{N}Hg^{II}_{S}(CSL9PenL23H)_3$ (PDB code 3PBJ). The copper is shown as an orange sphere, distances to the β-carbon of the residues being substituted are indicated for outer sphere substitutions: K22 (magenta), E24 (green) and K27 (yellow), and inner sphere: L19 (blue), and L26 (red).

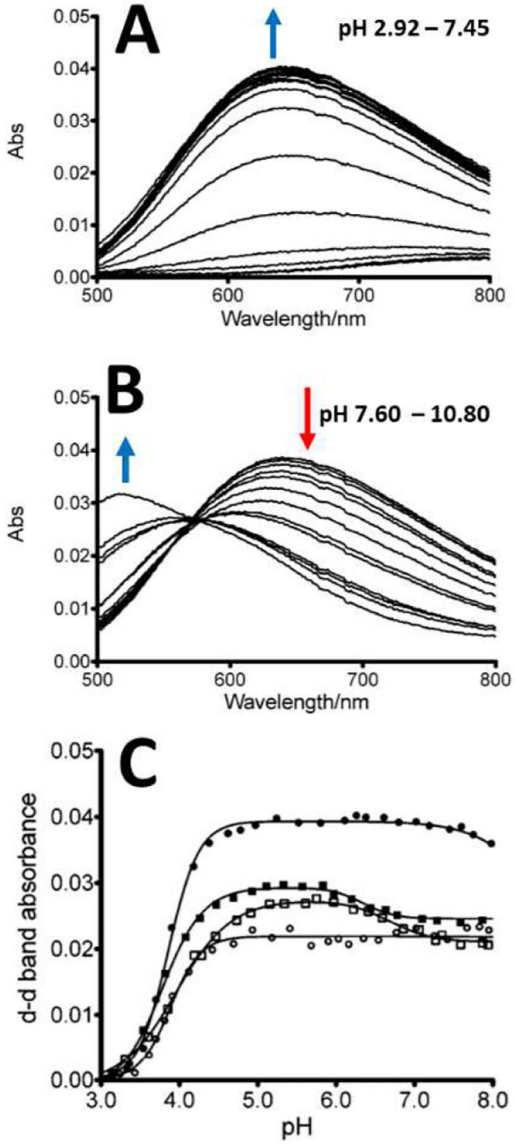

Figure 7:

pH titration of Cu(II)(TRI-H)$_3$ below (A) and above (B) pH 7.5. (C) Changes in Cu(II) d−d band absorbance when Cu(II) was bound to (●) TRI-H (Δcharge = 0); (○) TRI-EHE27K (Δcharge = 0); (■) TRIEH (Δcharge = −6); and (□) TRI-EHK24E (Δcharge = −12). Reprinted and adapted with permission from ref [50]. Copyright 2013 American Chemical Society.

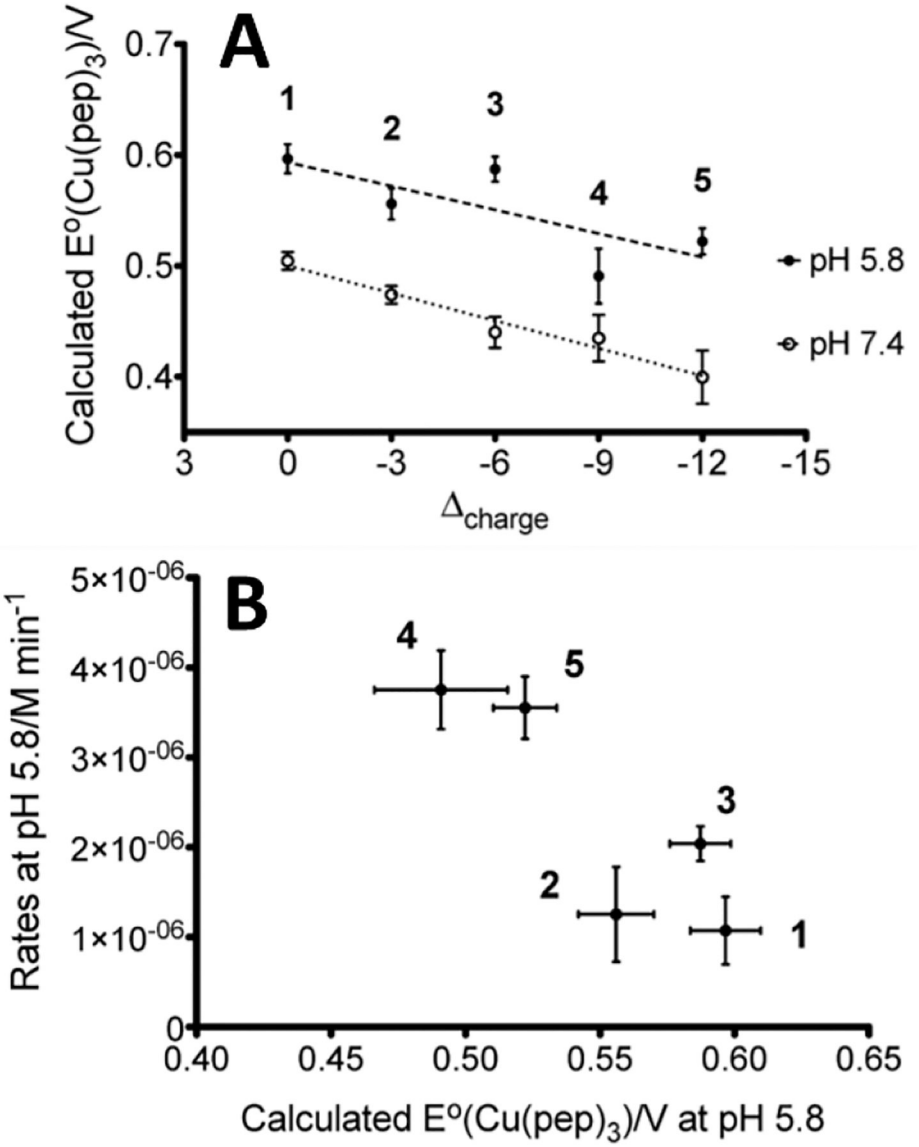

Figure 8:

Calculated reduction potentials in relation to the changes of the local charge at pH 5.8 and pH 7.4 (A). Rates of NiR activity vs. calculated reduction potentials at pH 5.8 (B). Peptides: (1) TRI-EHE27K; (2) TRI-EHE27Q; (3) TRI-EH; (4) TRI-EHK24Q; (5) TRIEHK24E. Reprinted and adapted with permission from ref [50]. Copyright 2013 American Chemical Society.

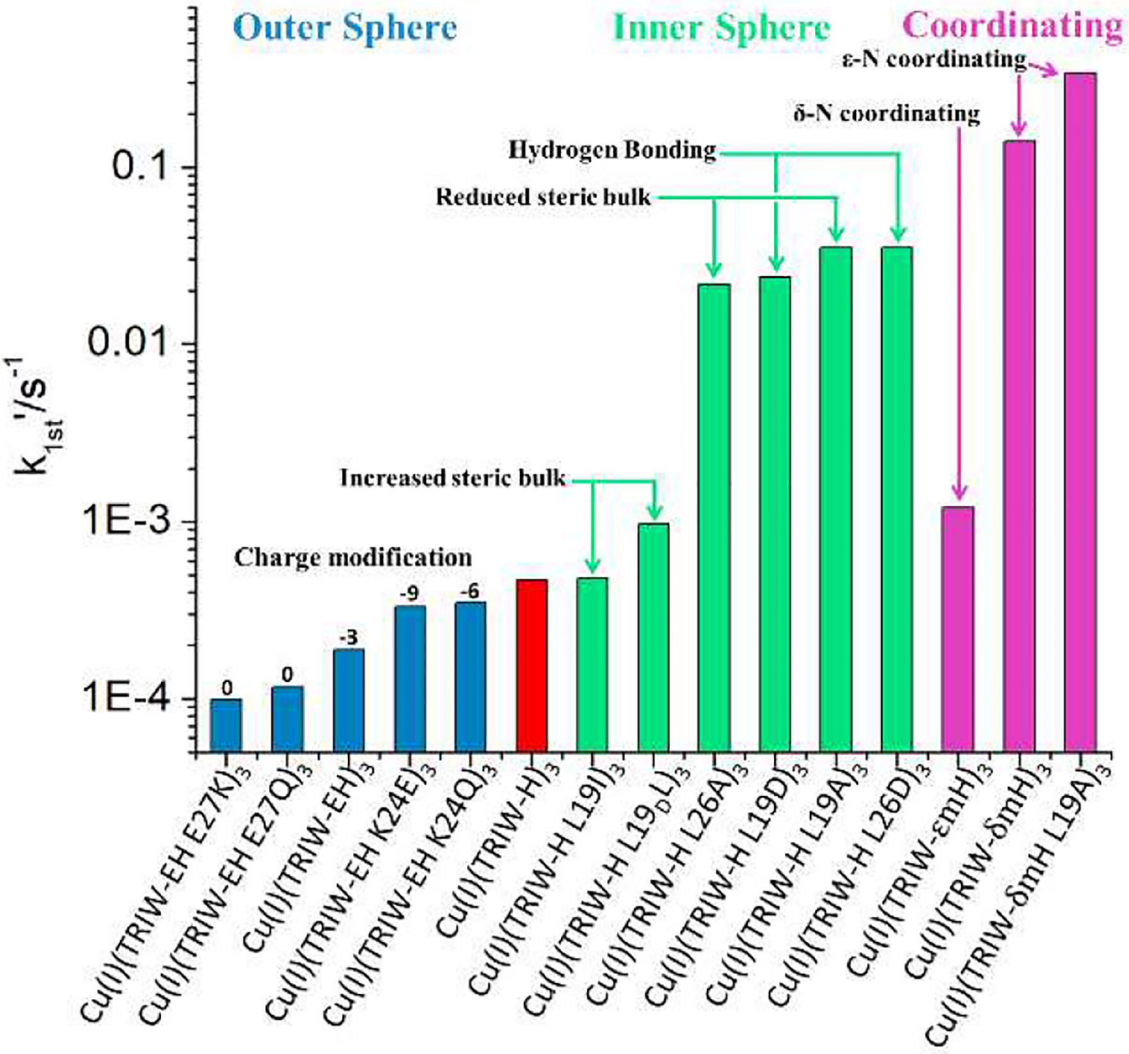

Figure 9:

Pseudo first order rate constants of the original TRIW-H construct (red) reported in ref[37] compared to the outer sphere helical interface residues (blue) reported in ref[50], interior residues (green) reported in ref[53], and primary coordinating residues (magenta) reported in ref[56]. Reprinted and adapted with permission from ref. [56]. Copyright 2019 American Chemical Society.

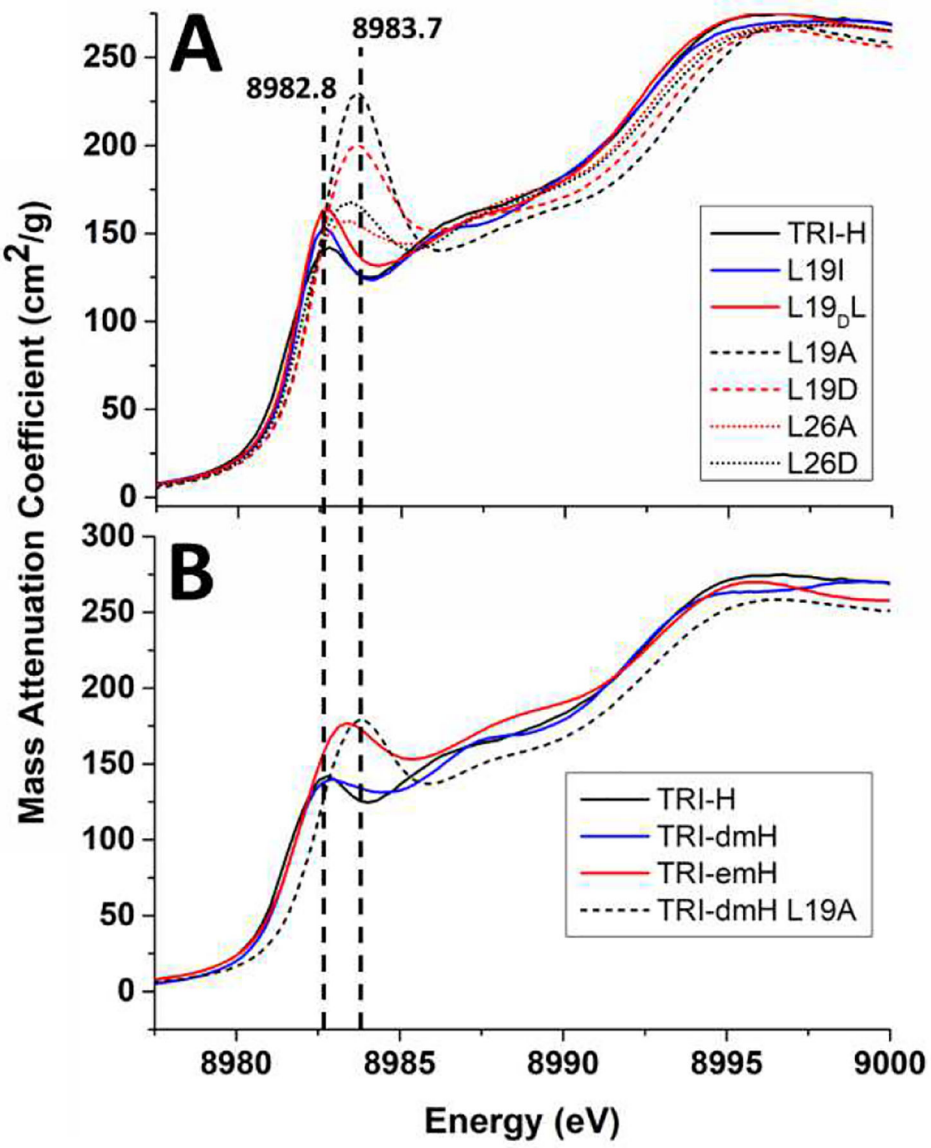

Figure 10:

Cu(I) XANES at pH 5.8 of inner sphere modifications (A) and primary coordinating modifications (B) reported compared to that of TRIW-H. Adapted and reprinted with permission from refs [53] and [56]. Copyright 2018 Angewandte Chemie International Edition and 2019 American Chemical Society.

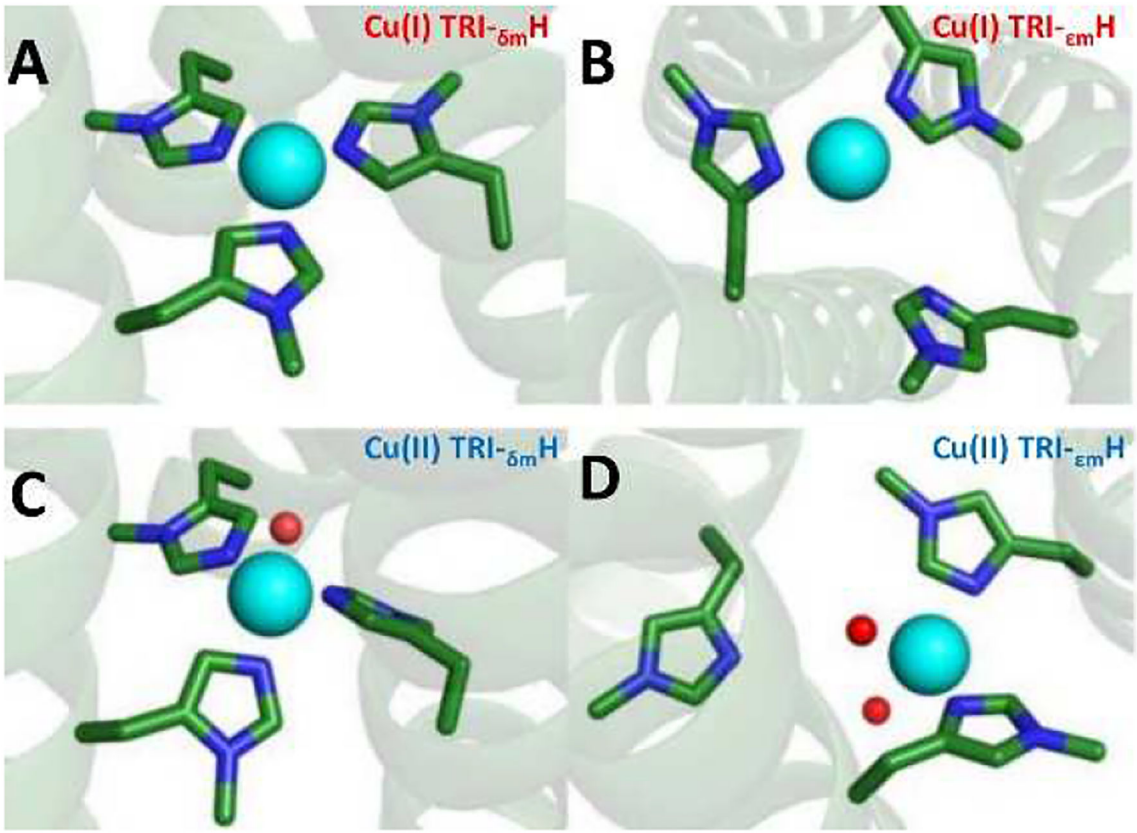

Figure 11:
Models of the metal binding sites of (A) Cu(I)-TRIW-δmH and (B) Cu(I)-TRIW-ɛmH (C) Cu(II)-TRIW-δmH and (D) Cu(II)-TRIW-ɛmH). Models were made using the program PyMol and based off the $Zn(II)(His)_3$ site of $Hg(II)_SZn(II)_N$ $(CSL9CL23H)_3$ [PDB 3PBJ[12]]. Reprinted and adapted with permission from ref. [56] Copyright 2019 American Chemical Society.

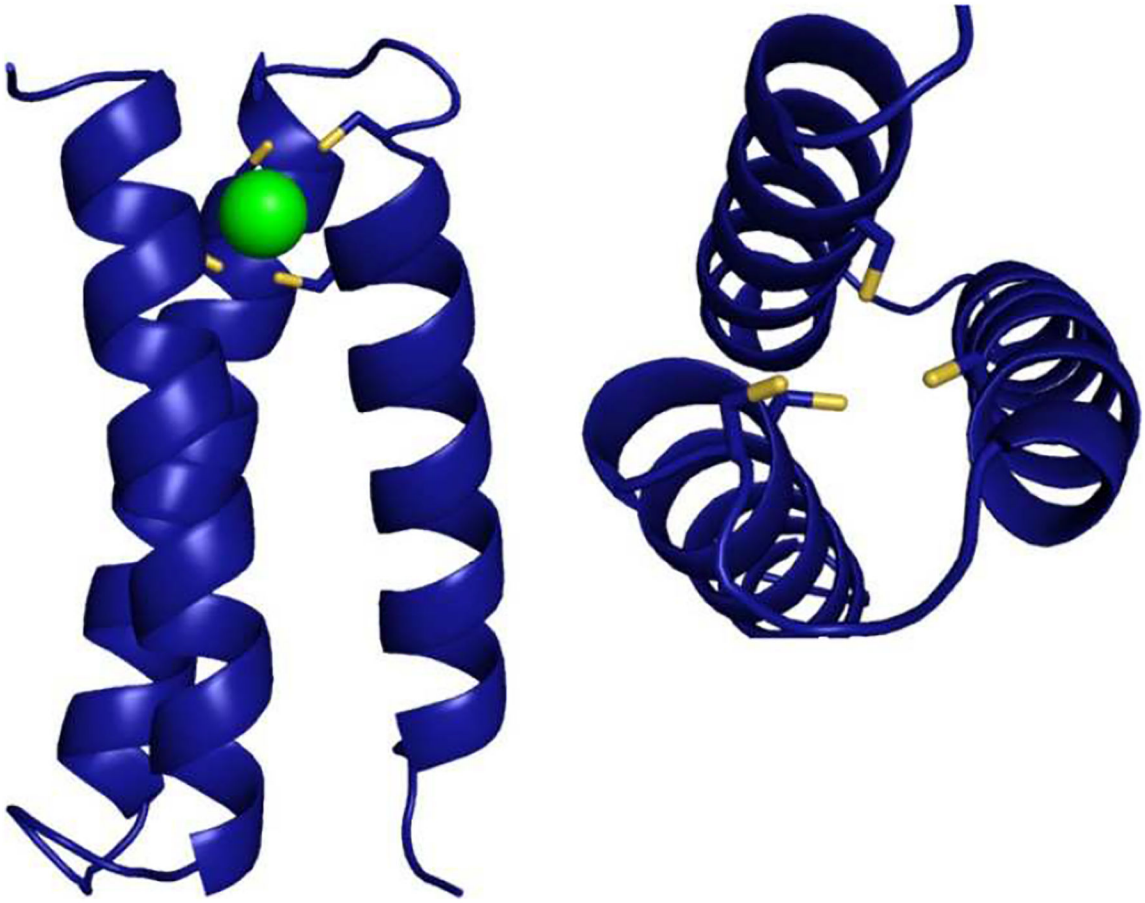

Figure 12:
Model of the synthetic rubredoxin, α3DIV-L21C-Fe, constructed in PyMol based on the NMR structure of α3DIV (PDB entry 2MTQ). Reproduced with permission from ref[67]. Copyright 2018 American Chemical Society.

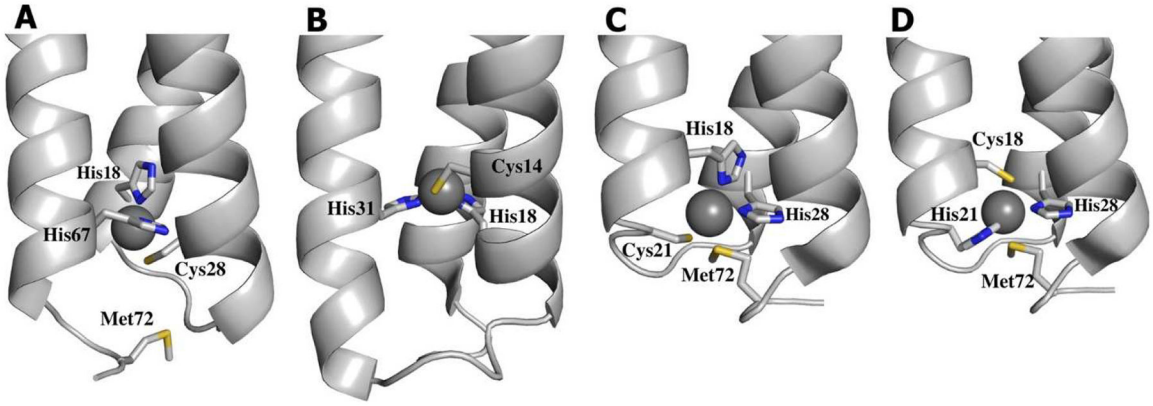

Figure 13:

Models of the reduced state based on the EXAFS analysis of the designed cupredoxins. (A) Cu(I) α_3DCR1. (B) Cu(I) α_3DChC2. (C) Cu(I) α_3DCH3. (D) Cu(I) α_3DCH4. Reproduced with permission from ref[79]. Copyright 2015 American Chemical Society.

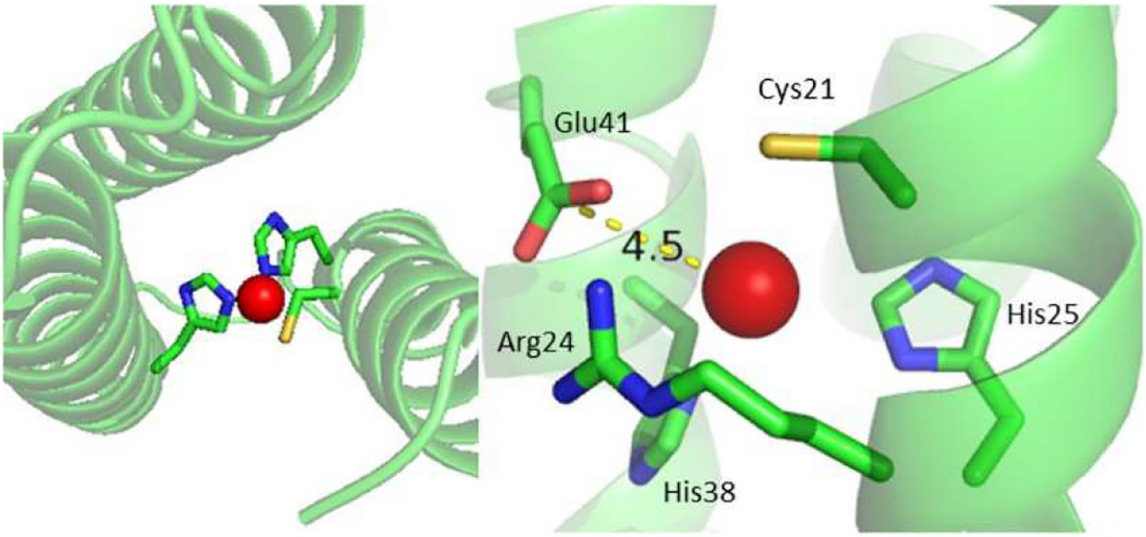

Figure 14:

PyMol illustrations showing the expected position of the metal binding site of GRα3DChC2 (left) and the expected Glu41–Cu distance if Cu(II) were bound in such a position. Reproduced with permission from ref[11]. Copyright 2018 American Chemical Society.

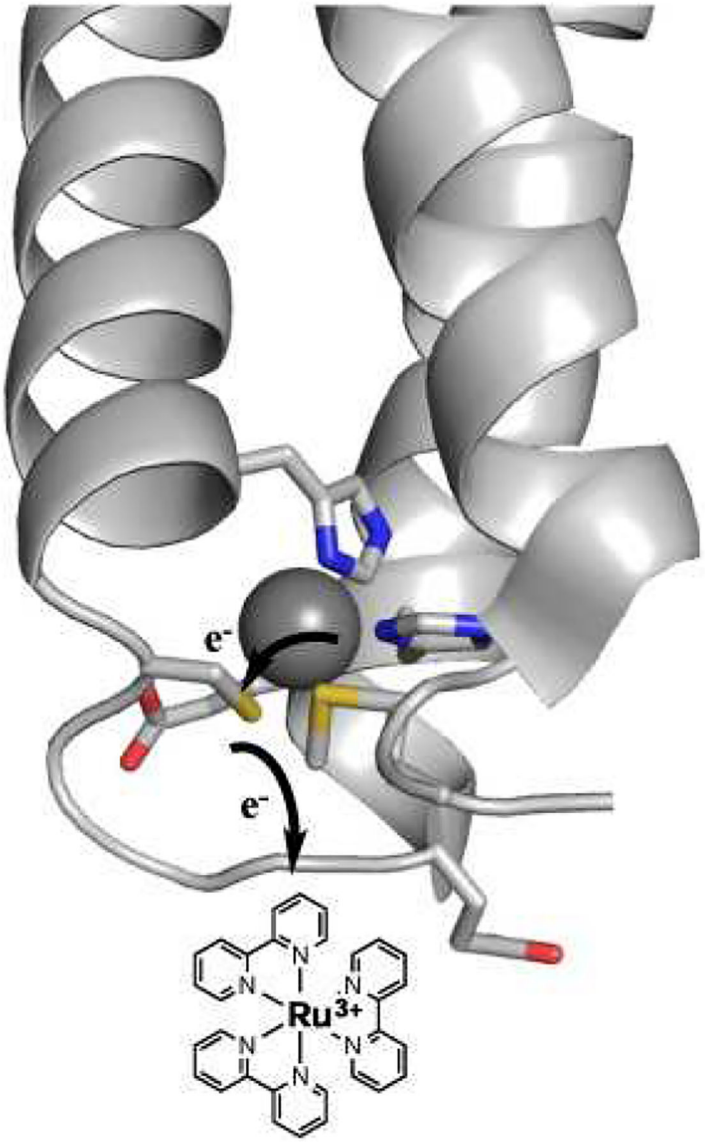

Figure 15:

Proposed electron transfer pathway. For Cuα3DCH3, the Cys residue can provide a super-exchange pathway for ET between the copper center and the photo-oxidant. Reproduced with permission from ref. Copyright 2018 Elsevier B.V.

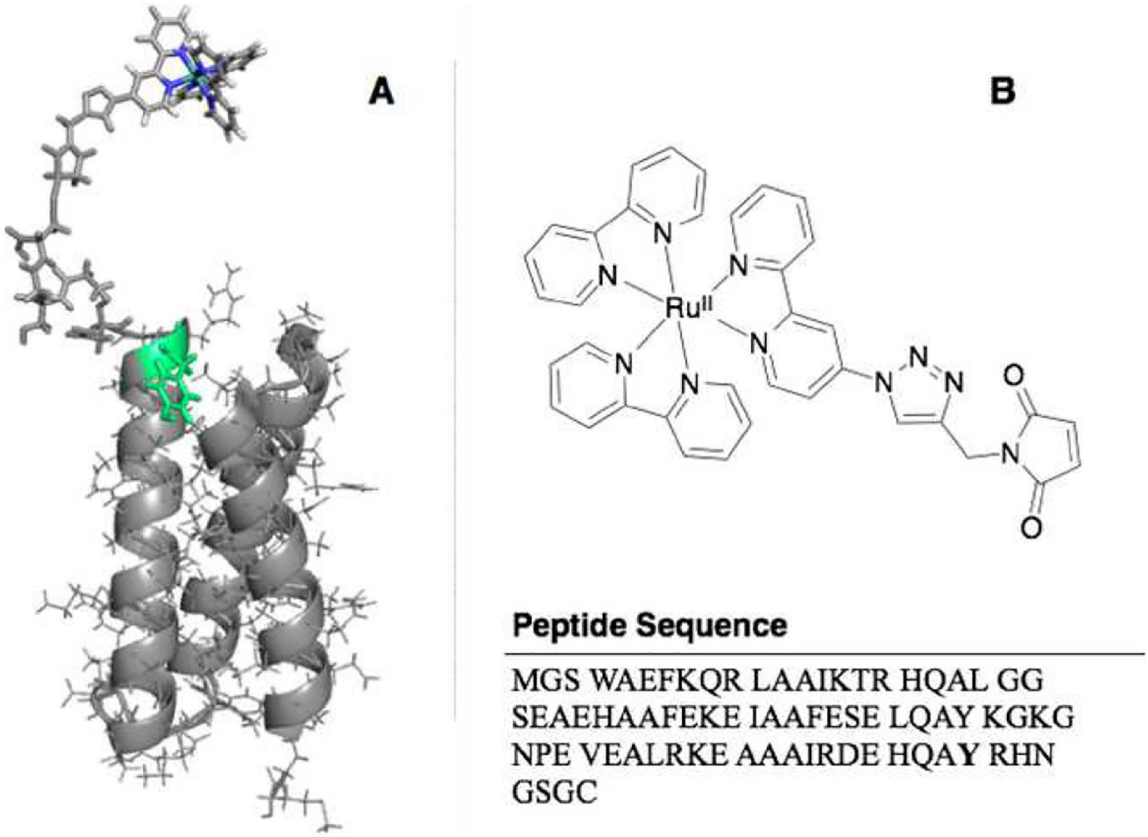

Figure 16:

A) Schematic representation of the structure of α_3DH_3-Rubpymal based on the solution NMR structure of a closely related scaffold (PDB: 2MTQ). The key tyrosine residue is marked in green. B) Chemical structure of Rubpymal (top) and sequence of α_3DH_3 (bottom). Reproduced with permission from ref[88b]. Copyright 2017 Wiley VCH.

Table 1:

List of parent peptide sequences discussed in this review.

Peptide[a]		**abcdefg**	**abcdefg**	**abcdefg**	**abcdefg**	
TRI	Ac-G	WKALEEK	LKALEEK	LKALEEK	LKALEEK	G-NH_2
CS	Ac-E	WEALEKK	LAALESK	LQALEKK	HEALEHG	-NH_2
Protein[b]	**loop**	**abcdefg**	**abcdefg**	**abcdefg**	**loop**	
α_3D	MGS	WAEFKQR	LAAIKTR	LQAL	GGS	
	EAE	LAAFEKE	IAAFESE	LQAY	KGKG	
	NPE	VEALRKE	AAAIRDE	LQAYRHN		

[a] N- and C-termini are acylated and amidated, respectively.

[b] Produced recombinantly in *e. coli.* (see ref. for details).

Table 2:

Kinetic parameters of pNPA hydrolysis of Zn-TRI peptides

Peptide Scaffold	pKa	k_{cat}/K_M (max) (M^{-1} s^{-1})[a]	k_{cat} (max) (s^{-1})
$[Zn]_N$(TRIL2WL23H)	9.2	25	~0.055
$[Hg]_S$ $[Zn]_N$(TRIL9CL23H)	9.0	31	~0.053
$[Zn]_N[Hg]_S$(TRIL9HL23C)	9.2	24	~0.030
$[Hg]_S[Zn]_N$(TRIL9CL19H)	9.6	27	~0.076

[a]Determined by fitting the pH dependent k_{cat}/K_M vs. pH data.

Table 3:

Kinetic parameters of CO_2 hydration by enzymes, small molecules, and our model scaffolds.

Enzyme / Model	pKa	pH	k_{cat} (s^{-1})	K_M (mM)	k_{cat}/K_M (L mol^{-1} s^{-1})	k_2 (L mol^{-1} s^{-1})	Ref
CAII	6.8[a]	8.8	8.2×10^5	8.9	9.2×10^7		[25]
CAIII	8.5	9.0	8×10^3	20	4×10^5		[26]
TRIL9CL23H	8.82[b]	9.5	1.8×10^3	10.0	1.8×10^5		[12]
α_3DH3	9.4	9.5	1.3×10^2	3.5	3.8×10^4		[24]
Zn^{II}([14]aneN4)	9.8					5040[c]	[27]
Zn^{II}([12]aneN4)	8.1					3012	[18a]
Zn^{II}(nitrilotris(2-benzimidazolylmethyl-6-sulfonate)	8.3					2180	[28]
Zn^{II}(tris(4,5-di-n-propyl-2-imidazolyl)phosphine)	8.0					2480	[29]

[a] Taken from ref [30]

[b] pKa of pNPA hydrolysis

[c] pH-independent second-order rate constant (maximal rate) calculated using pKa of 9.8 and measured rate of 690 M^{-1} s^{-1} at pH 9.0.

Table 4:

Peptide sequences of outer sphere (upper), inner sphere (middle), and primary coordinating (lower) residue substitutions for CuNiR activity studies. The position of these modifications can be viewed in Figure 6.

Peptide[a]		**abcdefg**	**abcdefg**	**abcdefg**	**abcdefg**		**Δ_{charge}**
TRI-H	Ac-G	WKALEEK	LKALEEK	LKALEEK	HKALEEK	G-NH_2	
TRI-HK22Q	Ac-G	WKALEEK	LKALEEK	LKALEEQ	HKALEEK	G-NH_2	−3
TRI-EH	Ac-G	WKALEEK	LKALEEK	LKALEEE	HKALEEK	G-NH_2	−6
TRI-EHE27K	Ac-G	WKALEEK	LKALEEK	LKALEEE	HKAKEEK	G-NH_2	0
TRI-EHE27Q	Ac-G	WKALEEK	LKALEEK	LKALEEE	HKAQEEK	G-NH_2	−3
TRI-EHK24Q	Ac-G	WKALEEK	LKALEEK	LKALEEE	HQALEEK	G-NH_2	−9
TRI-EHK24E	Ac-G	WKALEEK	LKALEEK	LKALEEE	HEALEEK	G-NH_2	−12
L19I	Ac-G	WKALEEK	LKALEEK	LKAIEEK	HKALEEK	G-NH_2	0
$L19_DL$	Ac-G	WKALEEK	LKALEEK	LKA_DLEEK	HKALEEK	G-NH_2	0
L19A	Ac-G	WKALEEK	LKALEEK	LKAAEEK	HKALEEK	G-NH_2	0
L26A	Ac-G	WKALEEK	LKALEEK	LKALEEK	HKAAEEK	G-NH_2	0
L19D	Ac-G	WKALEEK	LKALEEK	LKADEEK	HKALEEK	G-NH_2	−3
L26D	Ac-G	WKALEEK	LKALEEK	LKALEEK	HKADEEK	G-NH_2	−3
TRI-$_{\delta m}$H	Ac-G	WKALEEK	LKALEEK	LKALEEK	$_{\delta m}$HKALEEK	G-NH_2	0
TRI-$_{\varepsilon m}$H	Ac-G	WKALEEK	LKALEEK	LKALEEK	$_{\varepsilon m}$HKALEEK	G-NH_2	0
TRI-$_{\varepsilon m}$H L19A	Ac-G	WKALEEK	LKALEEK	LKAAEEK	$_{\varepsilon m}$HKALEEK	G-NH_2	0

[a] The N- and C-termini are acylated and amidated, respectively.

Table 5:

Kinetic parameters for CuNiR activity at pH 5.8 for select 3SCCs and small molecule model complexes

Construct	Rate (s^{-1})	V_{max} ($M\ S^{-1}$)	K_M (M)	k_{cat}(S^{-1})	k_{cat}/K_M ($s^{-1}\ M^{-1}$)
TRIW-H[58]	4.6×10^{-4}	N/A	N/A	N/A	N/A
TRIW-H L19A[59]	3.5×10^{-2}	$2.3 \pm 0.3 \times 10^{-6}$	0.24 ± 0.05	0.23 ± 0.03	1.0 ± 0.3
TRIW-$_{\delta m}$H	0.12	$1.5 \pm 0.1 \times 10^{-5}$	0.18 ± 0.02	1.5 ± 0.1	8.2 ± 0.1
TRIW-$_{em}$H L19A	0.30	$1.5 \pm 0.1 \times 10^{-5}$	0.13 ± 0.01	1.5 ± 0.1	11.3 ± 0.1
TRIW-$_{em}$H	1.2×10^{-3}	N/A	N/A	N/A	N/A
$[CuMe_2bpa(H_2O)(ClO_4)]^+$ on electrode pH 5.5[60] ref 65	N/A	N/A	1.1×10^{-3}	0.063	57.3
$[CuMe_2bpa(H_2O)(ClO_4)]^+$ in solution pH 5.5[60]	N/A	N/A	2.5×10^{-3}	5.3×10^{-5}	0.02
*Af*CuNiR pH 6.5[61]	N/A	N/A	1.5×10^{-4}	620	4.1×10^6
*Ax*CuNiR pH 7.0, 4 °C[62]	N/A	N/A	2.7×10^{-3}	89	3.3×10^5

The Rate value above refers to the pseudo-first order rate constant for metallopeptide-catalyzed reduction of nitrite by ascorbate in solutions containing 30mM nitrite and 1.2mM ascorbate.[58]

Table 6:

Physical properties of constructs reported in ref [67].

Protein	UV-Vis λ nm (ε M^{-1} cm^{-1})	Redox potential (vs. NHE)	Fe(III) Mössbauer (δ and ΔEQ in mm/s, D in cm-1, A in T)	Fe(II) Mössbauer (δ and ΔEQ in mm/s, D in cm-1, A in T)
Rubredoxin[69–70]	750 (350) 570 (3200) 490 (6600) 370 (7710)	−90 to +50 mV	$\delta/\Delta EQ$ = 0.24/−0.5, η = 0.2 D = +1.9, E/D = 0.23 $A_{xx,yy,zz}$ = (−16, −15.9, −16.9)	$\delta/\Delta EQ$ = 0.70/−3.25, η = 0.65 D = +7.4, E/D = 0.28 $A_{xx,yy,zz}$ = (−20.1, −8.3, −30.1)
α_3DIV L21C	595 (1200) 491 (2700) 345 (5000)	−75 mV (pH 8.5)	$\delta/\Delta EQ$ = 0.26/−0.5, η = 0.0 D = +0.5, E/D = 0.15 $A_{xx,yy,zz}$ = (−15.9, −16, −17)	$\delta/\Delta EQ$ = 0.73/−3.40, η = 0.9 D = +7, E/D = 0.26 $A_{xx,yy,zz}$ = (−16, −7.3, −25)

Table 7:

Physical properties of constructs reported in ref [79]

Protein	UV-Vis λ nm (ε M^{-1} cm^{-1})	EPR $A_{\parallel} \times 10^{-4}$ $_{cm}^{-1}$	Redox potential (mV vs. NHE)
α_3DCR1	380(1565), 550 (438), 600–800(300) $\varepsilon_{\sigma/\pi}$ = 3.6	163	+398
α_3DCH3	400(2619), 600–800(300) $\varepsilon_{\sigma/\pi}$ = 11.9	152	+364
α_3DCH4	377(1840), 450 (1098), 520(600), 600–700(380) $\varepsilon_{\sigma/\pi}$ = 3.3	185	+399
α_3DChC2	401(4429), 499 (2020), 600–700(550) $\varepsilon_{\sigma/\pi}$ = 2.2	130	+462
Plastocyanin[81]	460(400), 597(5200) $\varepsilon_{\sigma/\pi}$ = 0.05	63	+372
Ac Nitrite Reductase[40, 75]	457(2590), 570(1490) $\varepsilon_{\sigma/\pi}$ = 1.7	73	+247
Nitrosocyanin[76,82]	390(7000), 570(2200) $\varepsilon_{\sigma/\pi}$ = 3.2	144	+85

Table 8:

Physical properties of constructs reported in ref[11].

Protein	UV-Vis λ nm (ε M^{-1} cm^{-1})	EPR $A_{\parallel} \times 10^{-4}$ cm^{-1}	Redox potential (mV vs. NHE)
GRα$_3$DChC2	400(3760), 490(1600) $\varepsilon_{\sigma/\pi}$ = 2.3	142	+530
GRα$_3$DChC2R24A	399(2520), 490(1150) $\varepsilon_{\sigma/\pi}$ = 2.2	142	-
GRα$_3$DChC2R24M	399(3480), 493(1450) $\varepsilon_{\sigma/\pi}$ = 2.4	138	-
GRα$_3$DChC2E41Q	377(5120), 490(970) $\varepsilon_{\sigma/\pi}$ = 5.3	154	+510
GRα$_3$DChC2E41A	373(4090), 490(720) $\varepsilon_{\sigma/\pi}$ = 5.7	160	+510
Nitrosocyanin[76,82]	390(7000), 490(2200) $\varepsilon_{\sigma/\pi}$ = 3.2	142	+85

Table 9:

Intermolecular electron transfer properties of α_3DCH3

Sample	k_{1app} $\times 10^5$ s^{-1}	k_{2app} $\times 10^8$ M^{-1} s^{-1}	Driving Force (eV)
Apo α_3DCH3 + $Ru(bipy)_3$	0.39	3.9	
Cuα_3DCH3 + $Ru(bipy)_3$	1.15	6.3	1.18
Cuα_3DCH3 + $Ru(phen)_3$	1.07	10.7	0.88
Cuα_3DCH3 + $(COOEt)_4Ru(bipy)_3$	1.08	10.8	1.51
Cuα_3DCH3 + $(COOEt)_2Ru(bipy)_3$	1.05	10.5	1.24
Cuα_3DCH3 + ZnTMPyP	0.79	7.9	0.84